Fermi National Accelerator Laboratory

FERMILAB-Pub-97/377

# A Forward Proton Detector at D0

A. Brandt et al.

*Fermi National Accelerator Laboratory*
*P.O. Box 500, Batavia, Illinois 60510*

November 1997

Studies done in preparation of proposal Fermilab-P-900

Operated by Universities Research Association Inc. under Contract No. DE-AC02-76CH03000 with the United States Department of Energy

## Disclaimer



## Distribution

# A Forward Proton Detector at DØ

A. Brandt, A. Drozhdin, N. Mokhov
Fermi National Accelerator Laboratory

G. Alves, J. Barreto*, H. da Motta, M. Joffily, V. Oguri†, E. de Oliveira, A. Santoro, M. Souza
LAFEX, Centro Brasileiro de Pesquisas Fisicas, Rio de Janeiro, Brazil

N. Amos
University of Michigan

G. Snow
University of Nebraska

J. Blazey
Northern Illinois University

B. May, H. Schellman
Northwestern University

K. Mauritz
Iowa State University

October 31, 1997

**Abstract**

The addition of a Forward Proton Detector (FPD) as a new subdetector of the DØ detector for Run II is discussed. This document describes the physics motivation for the FPD as well as its location and performance.

*UFRJ–Universidade Federal do Rio de Janeiro, Brazil
†UERJ–Universidade Estadual do Rio de Janeiro, Brazil

# Contents

# 1 Introduction

This document discusses the construction of a Forward Proton Detector (FPD) as a new sub-detector of the DØ detector for Run II. The FPD uses machine magnets along with points measured on the track of the scattered proton to determine the proton momentum and angle.

Events with a leading proton comprise about 40% of the total cross section and are typically described by the exchange of a color-singlet pomeron, about which little is known. The addition of the FPD would facilitate studies of the structure of the pomeron and its dependence on diffractive mass and momentum transfer, determination of the quark and gluon content of the pomeron, search for diffractive production of heavy objects such as $W$ bosons, and studies of hard double pomeron exchange. These topics are ideally studied at the Tevatron due to the large center-of-mass energy available.

The FPD will consist of quadrupole spectrometers which tag outgoing protons or anti-protons with a minimum momentum transfer and a dipole spectrometer which detects anti-protons with a minimum momentum loss. The installation of the quadrupole spectrometers requires that minor modifications be made to the accelerator to create space for the detectors. Preliminary studies show that these modifications are feasible, but a full engineering study is necessary. The physics benefits of the quadrupole spectrometers include acceptance for a large range of proton momenta and tagging of both protons and anti-protons. This allows a full study of hard diffraction in regions of low background, detailed study of double pomeron events, and in addition provides samples of elastic scattering events for alignment and luminosity monitoring.

Small scintillating fiber detectors will be installed in a series of Roman pots to measure the $(x, y)$ coordinates of the proton or anti-proton track, thus allowing the determination of the track momentum and angle. The detectors will use multi-channel photomultiplier tubes which will be interfaced with Central Fiber Tracker trigger boards, resulting in DØ standard data structure and triggering. The FPD will not require any special running conditions and would have minimal impact on the standard DØ physics program except to broaden it.

The document is organized in the following manner. A discussion of the physics motivation is given in Sec. 2, followed by a description of the FPD in Sec. 3 and the hardware in Sec. 4. Triggering and data taking are covered in Sec. 5, followed by a section on accelerator modifications and conclusions.

# 2 Physics Motivation

## 2.1 Overview of Diffractive Physics

Quantum Chromo-Dynamics (QCD), the current theory for strong interactions, has been very successful at describing and predicting many areas of particle physics. Its successes are limited, however, to the perturbative regime where the strong coupling constant is small. About 40% of the total $p\overline{p}$ cross section at the Tevatron is elastic and diffractive scattering which are non-perturbative and cannot currently be calculated in QCD.

Figure 1(a) shows the diagram for elastic scattering in which a strongly interacting color singlet (pomeron) is exchanged resulting in the scattering of the proton and anti-proton. The right-hand side of the figure shows how a scattering would look in an ideal detector. The proton and anti-proton would be detected at extreme pseudorapidities[1] with a separation of 180° in azimuthal angle $\phi$. This figure also demonstrates the absence of associated particle production, or the rapidity gap, expected in elastic scattering due to the lack of color exchanged in the interaction. Figure 1(b) shows the diagram for diffractive dissociation, or single diffractive scattering, in which one of the beam particles (the proton in this case) has broken up, producing particles in the hemisphere of the detector opposite the detected $\overline{p}$.

The properties of elastic and diffractive scattering are well-described by the phenomenology of pomeron exchange (Regge theory), where the pomeron is a color singlet with quantum numbers of the vacuum. The literature on diffractive dissociation is extensive and a few review articles are given in Ref. [1]. Regge theory predates the quark-gluon model, and it is not clear how to combine it with QCD. Definitions of the pomeron vary from a theoretical definition: "the highest Regge trajectory with quantum numbers of the vacuum, responsible for the growth in the hadronic cross section with $\sqrt{s}$ " to an experimental one: "the thing that causes rapidity gaps" [2]. Many experiments have studied diffractive and elastic scattering at different center-of-mass energies, but due to the non-perturbative nature of the interactions, insight into the underlying process has been limited. The exact nature of the pomeron (Is it composed of quarks and gluons? hard or soft? the same object as a function of momentum transfer?) remains elusive, although recent theoretical ideas and experimental results are beginning to yield some answers. This brings us to the rather new field of hard

[1] Pseudorapidity, $\eta = -\ln\tan(\theta/2)$, where $\theta$ is the polar angle of the particle with respect to the beam, is frequently used as an approximation to rapidity.

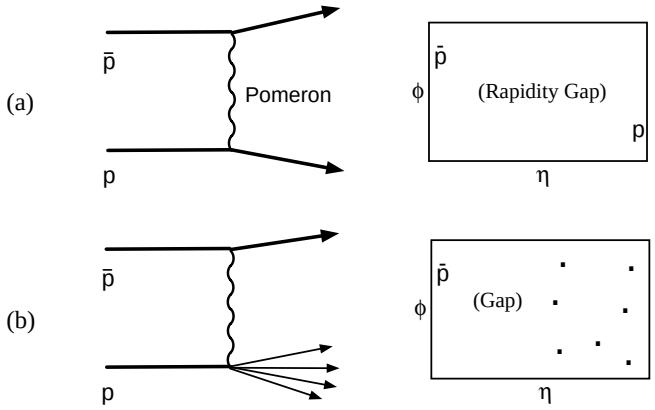


Figure 1: (a) The diagram for elastic scattering, in which a pomeron is exchanged resulting in the scattering of the proton and anti-proton. The $\eta$–$\phi$ plot shows the distribution of particles in this event—no particles are produced between the scattered proton and $\overline{p}$. (b) The diagram for single diffractive scattering, which is similar to elastic scattering except that the proton breaks up, producing particles in a limited region of rapidity.

diffraction.

### 2.1.1 Hard Diffraction

Ingelman and Schlein [3] proposed that the observation of jets in diffractive events would probe the partonic nature of the exchanged object, whether it is the pomeron or something else. Their paper introduced the field of hard diffractive scattering, which refers to the subset of traditional diffractive interactions characterized by high transverse momentum ($p_T$) scattering. They assumed that the pomeron can be treated as an object that exists within a proton, and that it is thus sensible to define a flux of pomerons in the proton as well as a pomeron structure function. They proposed a gluonic pomeron with either a hard structure, as would be derived from two gluons sharing the pomeron momentum $\sim \beta(1-\beta)$, or a soft structure like the gluonic structure of the proton $\sim (1-\beta)^5$, where $\beta$ is the momentum fraction of the parton with respect to the pomeron. With these assumptions they were able to make predictions for diffractive jet production cross

sections and properties.

The first experimental results on this subject were published by the UA8 Collaboration at CERN, and showed the existence of jets in single diffractive events [4] and that these jets had rapidity and longitudinal momentum distributions consistent with a hard pomeron structure [5]. There was also evidence for a "super-hard" or "coherent" pomeron, where the entire momentum of the pomeron participates in the hard scattering [5].

The UA8 Collaboration tagged diffractive events using a small angle spectrometer to detect and reconstruct the leading proton [6]. A proton spectrometer typically consists of machine magnets surrounded by a series of Roman pots, which are vessels that house position detectors. These pots can be positioned close to the beam and used to measure protons that are scattered through small angles, by measuring the bend of the track in the known magnetic field. Diffractive events can also be identified using rapidity gaps [7, 8], which are experimentally defined as the absence of particles or energy above threshold in some region of rapidity. Since the pomeron is a color singlet, radiation is suppressed in events with pomeron exchange typically resulting in large rapidity gaps in these events [9].

Figure 2 shows the diagram for hard single diffraction producing two jets, a scattered $\overline{p}$, and a rapidity gap. This figure is identical to Fig. 1(b) for traditional diffraction except for the production of jets. We use the convenient language of Ingelman and Schlein to describe the process as occurring in two steps. First the pomeron is emitted from the $\overline{p}$, with an emission probability described by the pomeron flux factor. The $\overline{p}$ is scattered but remains intact, while the pomeron interacts with the proton in a hard scattering producing jets and a rapidity gap in the region near the $\overline{p}$. The charge conjugate diagram where the proton remains intact and the $\overline{p}$ is fragmented is equally likely. The detailed study of these interactions will yield insight into the nature of the pomeron and reveal the validity of this phenomenological picture.

### 2.1.2 Recent Experimental Results

The study of hard diffractive processes has expanded dramatically in recent years. Results from HERA and the Tevatron include the observation of diffractive jet production [10, 11, 12], diffractive $W$ boson production [13], and rapidity gaps between high transverse energy jets [14, 15, 16, 17].

As an example of some of this work, we describe in detail a DØ search for hard diffractive jet production using rapidity gap techniques. Preliminary

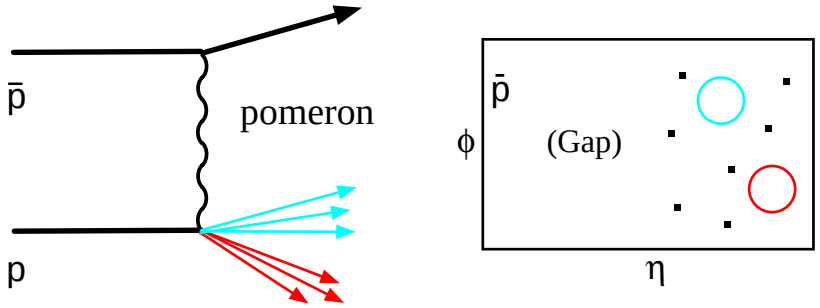


Figure 2: The diagram for a hard single diffractive interaction resulting in a final state with a scattered $\overline{p}$ and two jets. The $\eta$–$\phi$ plot shows the distribution of particles in this event including a rapidity gap near the scattered $\overline{p}$ and the circles which represent the two jets.

results show evidence for hard diffractive jet production at center-of-mass energies $\sqrt{s}$ = 1800 GeV and 630 GeV [11]. The data used in this study were obtained using a forward jet trigger requiring at least two jets above 12 GeV in the region $\eta > 1.6$ or $\eta < -1.6$. A forward jet trigger is ideal for studying diffractive jet production, since the interacting parton in the pomeron typically has a smaller momentum fraction than the one from the proton, resulting in a boosted jet system. Events with multiple $p\overline{p}$ interactions or spurious jets have been removed. Jets are reconstructed using a cone algorithm with radius $R = \sqrt{\Delta\eta^2 + \Delta\phi^2} = 0.7$. The number of EM towers ($n_{EM}$) above a 200 MeV energy threshold is measured opposite the leading two jets ($E_T > 12$ GeV) in the region $2 < |\eta| < 4.1$ for the data. The ($n_{EM}$) distribution is shown in Fig. 3 for $\sqrt{s}$ of (a) 1800 GeV and (b) 630 GeV. The distributions at both center-of-mass energies show a striking peak at zero multiplicity indicating a class of events with no particles detected opposite the dijet system. The curves shown are negative binomial fits to the data excluding low multiplicity bins and extrapolated to zero to estimate the background from standard color exchange, which is typically well described by such a distribution [18]. The dashed curve is a fit to the whole distribution, while the dotted curve is a fit to the leading edge only. The excess at zero multiplicity for both center-of-mass energies is on the order of 1% and is in qualitative agreement with expectations for a hard diffractive component.

Figure 4(a) shows an actual DØ hard diffractive candidate event with Roman pots superimposed. This overlay demonstrates how a "typical" Run II event display might appear: a central jet, a forward jet, calorimeter energy and charged tracks in one hemisphere, and a rapidity gap and detected antiproton in the other hemisphere. Figure 4(b) shows a similar overlay with a hard double pomeron exchange candidate (extracted from a promising preliminary search for this class of events described in Ref. [11] and Sec. 2.2.4), which has two central jets and forward–backward rapidity gaps. Both $\overline{p}$ and $p$ tracks could be detected in this event with the Forward Proton Detector, the details of which will be discussed later in this document.

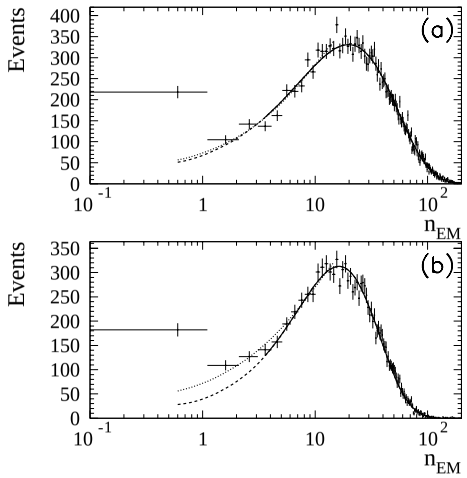


Figure 3: Number of electromagnetic calorimeter towers ($n_{EM}$) above a 200 MeV energy threshold for the region $2 < \eta < 4.1$ opposite the forward jets for center-of-mass energies of (a) 1800 GeV and (b) 630 GeV. The curves are negative binomial fits to the data excluding low multiplicity bins.

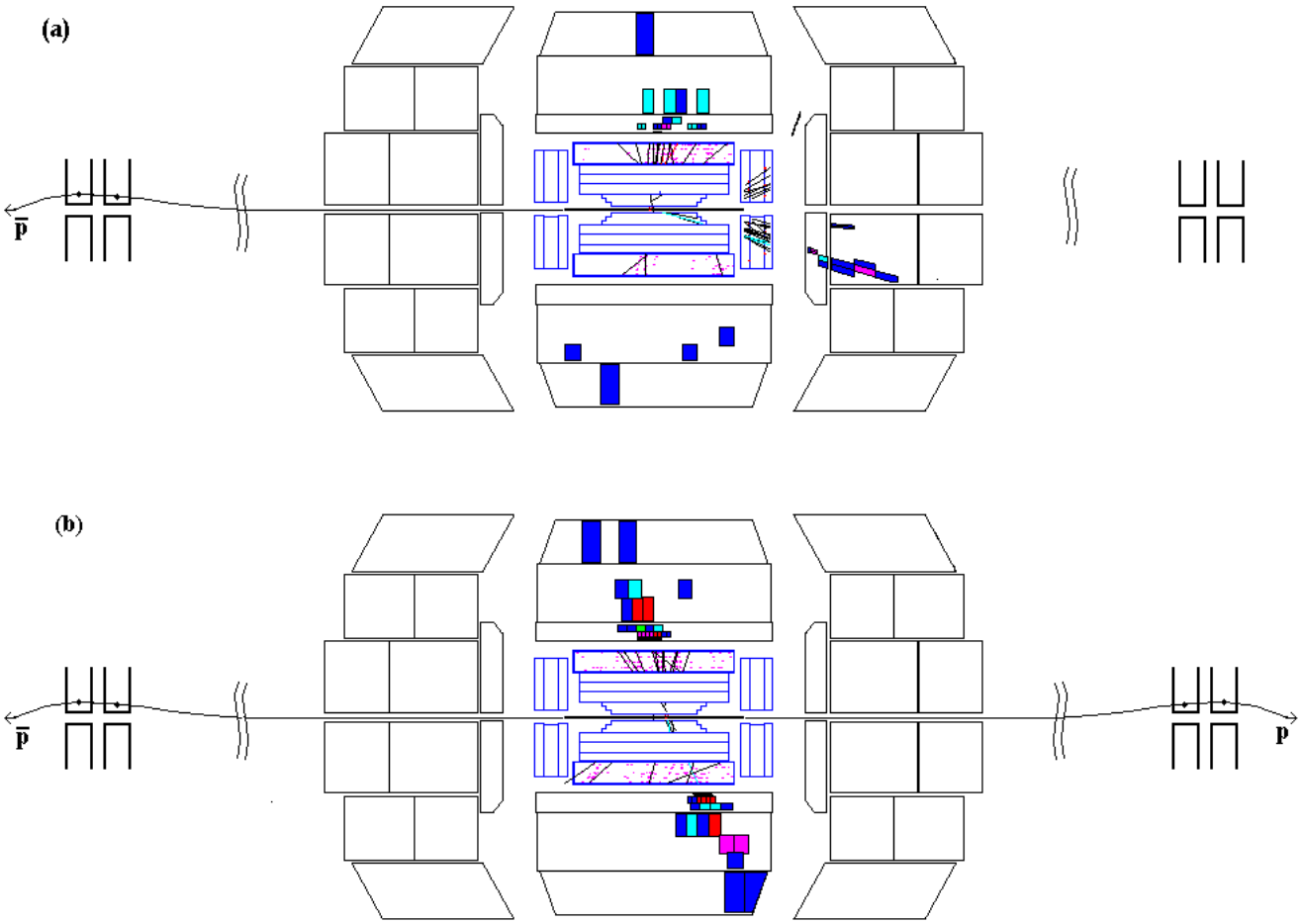


Figure 4: Event displays showing Run I candidate events with a Forward Proton Detector (not to scale) added. (a) shows a hard diffractive candidate with a forward and central jet and a large rapidity gap in the out-going $\overline{p}$ hemisphere. The $\overline{p}$ could be tagged by the FPD. (b) shows a hard double pomeron candidate event with central jets and two rapidity gaps. Both the $p$ and $\overline{p}$ could be tagged with the FPD.

The H1 and ZEUS Collaborations have published many papers on diffraction, and the combination of diffractive jet production with diffractive deep inelastic scattering measurements has led to a picture of the pomeron that is dominantly composed of hard gluons, but with some quark component [19]. Results from CDF on hard diffractive jet production (similar to the DØ analysis detailed above), combined with their observation of diffractive $W$ boson production, also support a dominantly gluonic Pomeron, but do not yield much insight into the pomeron structure function. There are also questions about how to combine results from HERA and the Tevatron, as the normalization may depend on center-of-mass energy [20]. The normalization uncertainty arises from how the flux of pomerons in the proton is defined and whether or not the pomeron obeys the momentum sum rule, which states that the sum of the momentum fractions of the constituents of a particle should be one. The momentum sum rule is not obviously true for the pomeron, which may not be a traditional particle with a uniquely defined structure function. The data obtained with the FPD should shed light on many of these issues and lead to a coherent picture of the pomeron.

## 2.2 Physics Topics Accessible with the FPD

### 2.2.1 Diffractive Mass Dependence

Although rapidity gap studies can be used to gain some insight into the nature of the pomeron, these studies can be vastly improved through the addition of a Forward Proton Detector (FPD). Tagging the forward proton removes the ambiguity of a rapidity gap tag, which suffers from background due to low multiplicity non-diffractive events. This removes the need for fitting multiplicity distributions to determine the non-diffractive background (as shown in Fig. 3). The rapidity gap tag also does not give information on whether the scattered proton remains intact or is excited into a low-mass state, which could still yield a rapidity gap.

By detecting the scattered proton, one can measure its momentum (p) and thus derive two key variables $x_p = \mathrm{p}/\mathrm{p}_{\mathrm{beam}}$, the fractional longitudinal momentum of the scattered proton, and $t = (\mathrm{p}_{\mathrm{beam}} - \mathrm{p})^2$, the four-momentum transfer to the proton. Rapidity gap techniques do not give access to these two variables and thus lose important information about the diffractive process. The momentum fraction of the pomeron ($\xi$) is simply related to the momentum fraction of the proton by $\xi = 1 - x_p$. A measurement of the proton momentum thus gives the diffractive mass $M_X$ through

the equation $M_X = \sqrt{\xi} \cdot \sqrt{s}$, where $\sqrt{s}$ is the center-of-mass energy.

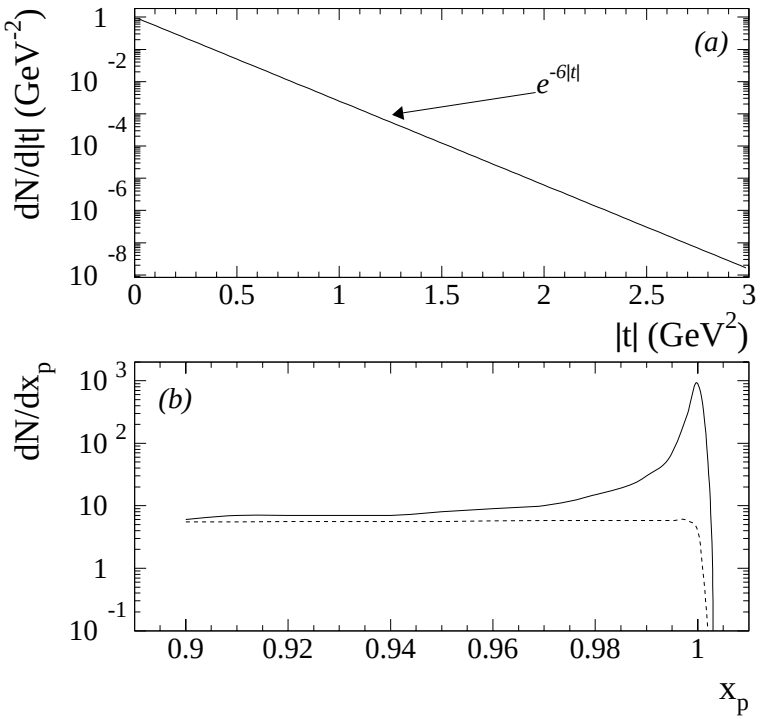


Figure 5: (a) A plot of $\mathrm{d}N/\mathrm{d}|t| = e^{-6|t|}$ which is a good approximation to the $|t|$ distribution for single diffraction. (b) The solid curve shows an approximation to the $x_p$ dependence of CDF single diffractive data. The dashed curve shows an estimate of the non-pomeron exchange background.

Figure 5(a) shows the $|t|$-dependence of single diffraction, which has been measured to be $d\sigma/d|t| \sim e^{-b|t|}$, where $b \approx 6$ for single diffraction at $\sqrt{s} =$ 1800 GeV [21]. The exact slope has a mild dependence on $\sqrt{s}$ and $M_X$. For elastic scattering, the cross section drops even more steeply with $b \approx 17$ [22]. Figure 5(b) shows the $\xi$ dependence of diffraction, where the curves are approximations to the $\sqrt{s} = 1800$ GeV data in Ref. [21]. The solid curve is sharply peaked at $\xi = 0$ (the beam energy), with some smearing due to the 0.1% momentum resolution and a tail to higher $\xi$ values (the distribution for elastic scattering does not have the higher $\xi$ tail). The dashed curve is an estimate of the non-pomeron exchange background. Pomeron exchange

is typically assumed to dominate over other exchanges in the region where $\xi < 0.05$ ($x_p > 0.95$), which implies a maximum mass of $M_X = 450$ GeV/$c^2$ for the Tevatron in Run II ($\sqrt{s} = 2000$ GeV).[2]

The ability to obtain large data samples and divide the data into mass bins facilitates the comparison of the data with theory in the form of phenomenological Monte Carlos, and allows studies of the pomeron structure in the pomeron-proton center-of-mass.

### 2.2.2 Momentum Transfer Dependence

The ability to study hard diffraction in bins of momentum transfer is another crucial advantage provided by the FPD. The momentum transfer to the proton is equal to the momentum transfer of the pomeron, and there is a simple relation between the momentum transfer and the angle $\theta$ of the scattered proton $\theta = \sqrt{t}/(\mathrm{p_{beam}} \cdot \sqrt{x_p})$. Current phenomenology assumes that the slope of $d\sigma/dt$ is the same as for soft diffraction, but this requires verification. It is quite possible that a phase transition in the behavior of the pomeron occurs above some $|t|$ threshold. At low $|t|$, the pomeron structure may be significantly softer (that is, peaked at lower $\beta$) than at higher $|t|$, where it may have a hard two gluon or two quark structure which results in intermediate $\beta$, or a super-hard structure (like a single gluon) which results in a $\beta$ distribution peaked near one.

### 2.2.3 Super-hard Pomeron

One limitation of rapidity gap techniques is that the requirement of a rapidity gap reduces the fiducial volume of the detector. The use of a scattered proton as the diffractive tag, on the other hand, allows the full rapidity range of the detector to be exploited to study the diffractive system. This would in turn allow a search for the effects of the super-hard pomeron, which is expected to frequently result in back-scattered jets in the rapidity interval normally used to tag rapidity gaps. The super-hard pomeron is of great theoretical interest [23], part of which stems from the fact that if the entire pomeron momentum participates in the hard scatter, there is a dramatic increase in the cross section for the diffractive production of heavy objects, such as $b$ quarks [24]. The cross section for hard double pomeron exchange is also enhanced by super-hard pomeron exchange [25, 26].

[2] This rule of thumb is derived from lower $\sqrt{s}$ experiments, and Fig. 5(b) indicates $\xi < 0.03$ ($M_X = 350$ GeV/$c^2$) might be a safer requirement to avoid background.

### 2.2.4 Hard Double Pomeron Exchange

Hard double pomeron exchange is another process that can be studied effectively using the FPD. In this process both the incoming proton and anti-proton emit a pomeron and the two pomerons interact to produce a massive system. At the Tevatron a central system of about 100 GeV could be produced. With both arms instrumented it would be possible to measure both the proton and anti-proton using the FPD, and jets (for example) using the central calorimeter.

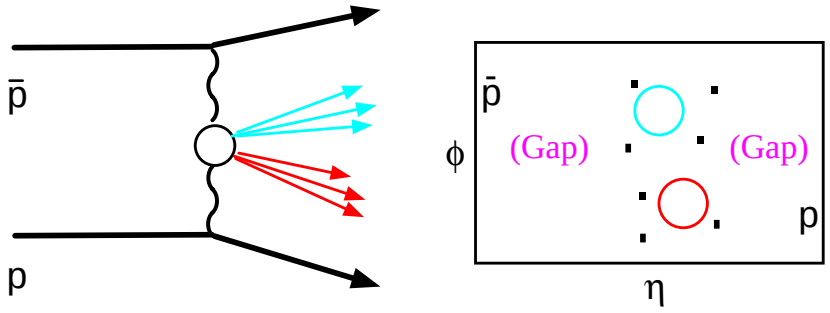


Figure 6: The diagram for a hard double pomeron exchange interaction resulting in a final state with a scattered proton, anti-proton, and two jets. The $\eta$–$\phi$ plot shows the distribution of particles in this event including forward and backward rapidity gaps and the circles which represent the two jets.

Due to the lack of color flow, rapidity gaps are expected to be produced whenever a pomeron is emitted. Hard double pomeron exchange would thus be expected to produce two rapidity gaps in conjunction with central jets. DØ has already begun a search for this unique topology, which is shown in Fig. 6. A sample of double gap events has been observed, although the interpretation of them in terms of hard double pomeron exchange requires further study [11]. The addition of the FPD would remove any ambiguity from these results and make it possible to study these very interesting events in detail as the kinematics of the event would be fully determined by the detection of both the $p$ and $\overline{p}$.

Observation and measurement of hard double pomeron exchange would help determine the pomeron structure and provide unique information on

the pomeron flux. Double pomeron exchange would have a normalization proportional to the square of the flux factor, unlike other hard diffractive processes. In addition, this process has been proposed as a trigger for Higgs production at the LHC [27]. Knowledge gained at the Tevatron would indicate if this approach is worth pursuing.

### 2.2.5 Diffractive Production of Massive States

Hard diffraction is not limited to jet production. As mentioned earlier, there is already evidence for diffractive $W$ boson production [13]. There is now preliminary evidence for diffractive $b$ quark and $J/\Psi$ production as well [28]. It is plausible that every state below mass threshold can be produced diffractively, so diffractive production of Higgs bosons and top quarks is not out of the question. The FPD combined with the excellent particle identification of the upgraded DØ detector will allow searches for a large range of hard diffractive final states. Combining the information from different diffractive searches will allow the determination of the quark and gluon content of the pomeron, as well as testing whether it behaves like a universal object with a consistent structure.

### 2.2.6 Other Physics Topics

There are many other physics topics besides hard diffraction that will be accessible with the FPD. These include

- Inclusive double pomeron. This process has not been observed at the Tevatron and there are large uncertainties in the cross section. Recent predictions of shadowing effects [29] can be tested as well as the pomeron flux factor. Inclusive double pomeron interactions are an ideal place to look for glueball production, and the clean event topologies would make them easier to detect.

- Centauros. The observation of anomalous cosmic ray events [30] has not been adequately explained. It has been proposed that centauros may be produced diffractively, which would explain why they have not yet been observed by collider experiments [31]. The FPD would allow the search for centauro production in diffractive events.

- High-$|t|$ elastic scattering. There is little data on elastic scattering except at small momentum transfers, so the FPD would be in a unique

position to map out the $|t|$ dependence of the elastic cross section up to a few GeV$^2$.

- Inclusive single diffraction. Many properties of inclusive single diffraction have been measured at the Tevatron [21], but there is little data on the momentum transfer dependence of these results. The FPD will allow us to make significant contributions to the understanding of soft as well as hard diffraction.

- Comparison of results with different tags. Combining rapidity gap tags and proton tags will also be an interesting study to see how often the proton is associated with a rapidity gap and vice versa. Complete overlap is not expected due to the super-hard pomeron, which would not generally give a rapidity gap in the DØ detector, and also due to diffractive excitation of the proton.

### 2.3 Tevatron versus HERA

Although much can be learned about the pomeron at HERA, there are distinct advantages to studying hard diffraction at the Tevatron. Diffractive systems with mass greater than 450 GeV/$c^2$ can be produced at the Tevatron compared to only 70 GeV/$c^2$ at HERA. This allows for the production of high $p_T$ objects at the Tevatron (such as $W$ or $Z$ bosons) as well as large jet cross sections. Without these large cross sections it is impossible to study high $|t|$ exchange since the cross section decreases so steeply with $|t|$ (Fig. 5). The super-hard pomeron can best be studied at the Tevatron, since at HERA it can result only from a higher twist diagram, which is suppressed (gluons from the pomeron cannot connect directly to the photon, but must connect to the hard scattering, a configuration which is suppressed) [32]. Double pomeron exchange obviously cannot be studied at an $ep$ collider. Finally, one of the key results will stem from the comparison of pomeron structure in $ep$ and $p\bar{p}$ collisions. If the pomeron behaves like a particle it should have consistent structure independent of the nature of the probe (electron or proton).

### 2.4 Interpretation of the Data

To effectively utilize the large data samples that can be obtained with the FPD (see Sec. 5), it is useful to have Monte Carlo simulations of the physics processes. The Monte Carlo POMPYT [33] incorporates the Ingelman-Schlein

model (described in Sec. 2.1.1) and can be used to generate samples to compare to hard diffractive data. The Monte Carlo allows for the choice of different pomeron structure functions and quark and gluon combinations, and can thus be used in conjunction with the data to derive a pomeron structure, or to determine if the concept of a pomeron structure is valid.

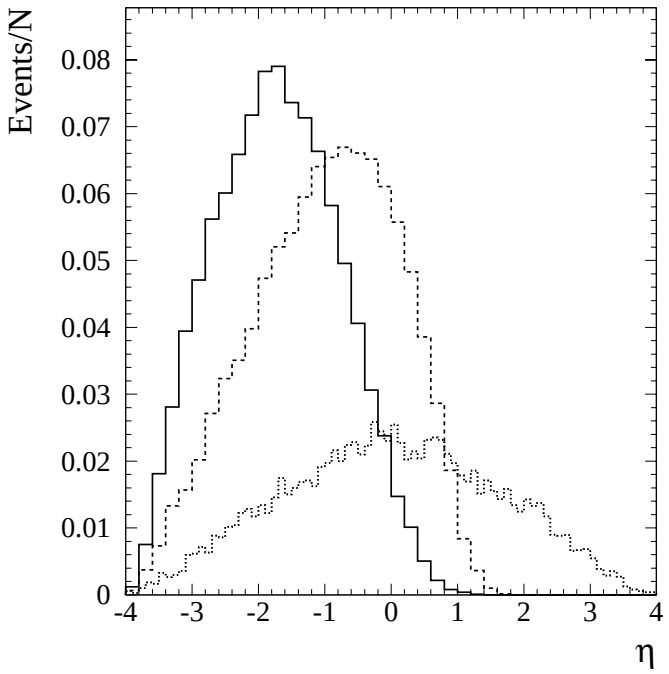


Figure 7: The pseudorapidity distribution of the two leading (highest $E_T$) jets for Monte Carlo simulations. The solid (dashed) histogram is from the POMPYT hard diffractive Monte Carlo with a scattered proton at $\eta \approx 8$ and a soft (hard) gluonic pomeron structure. The dotted histogram is from the non-diffractive PYTHIA Monte Carlo.

We have performed Monte Carlo studies of diffractive dijet production. Figure 7 shows the $\eta$ distribution of the leading two jets ($E_T > 12$ GeV) for three Monte Carlo samples. The solid and dashed histograms are generated using POMPYT with soft and hard pomeron structures, respectively, while the dotted histogram is for a non-diffractive PYTHIA [34] sample. This vari-

able clearly has sensitivity to different pomeron structures, with the softer structure boosted significantly towards negative $\eta$ (the direction opposite the detected proton) compared to the hard structure and the symmetric PYTHIA distribution. This variable and similar variables, such as the longitudinal momentum of the two jet system (which directly reflects the imbalance between the parton from the pomeron and the parton from the proton), can be used to derive the pomeron structure. Event samples of a few hundred events are adequate to distinguish between a hard and soft structure (as done in UA8), but larger samples will allow the detailed extraction of a pomeron structure in various $\xi$ and $|t|$ bins. These variables, however, cannot distinguish easily between a quarkonic or a hard gluonic pomeron, which have similar structures.

To derive the quark and gluon content of the pomeron, we will want to measure the dijet cross section as well as the cross section for other process, such as diffractive $W$ boson and diffractive $b$ quark production. These processes have different dependences on the quark and gluon content of the pomeron, as well as the pomeron structure function. Measuring the cross section thus gives complementary information to that obtained from various angular and kinematic distributions. An example of the power of the cross section to distinguish between different pomeron models is the measurement of the dijet cross section for two jets with $E_T > 20$ GeV. The prediction for a hard gluon cross section is 2.3 times the hard quark cross section, with little $\eta$ or $E_T$ dependence, while the soft gluon ranges from about 0.5 to 3.0 times the hard gluon depending on the exact $\eta$ and $E_T$ cuts. From our experience in Run I, we expect to be able to measure this cross section with a better than 50% error. If we have enough statistics to raise the $E_T$ threshold, the error can be reduced to about 30%.

There are currently no double pomeron Monte Carlos, but we are working on modifying POMPYT to simulate hard double pomeron exchange. Jon Pumplin and John Collins also are interested in incorporating their double pomeron models into Monte Carlos and we expect to have more and better predictions over the next couple of years. The final word will of course be given by the unique data samples obtained with the FPD.

## 2.5 Physics Motivation Summary

The dramatically expanding field of hard diffraction has been driven by experimental results and experiment should continue to lead theory. More precise results are needed to improve the understanding of the nature and

structure of the pomeron and distinguish between different theoretical models. There is a rich, timely program of physics that can be accessed with the addition of the FPD to the DØ detector. This includes

- Studies of pomeron structure using diffractive jet production, including the dependence on $\xi$ and $|t|$.
- Search for diffractive production of heavy objects and combining different hard diffractive channels to determine the quark and gluon content of the pomeron.
- Search for the super-hard pomeron.
- Studies of double pomeron exchange.
- Search for "new physics" such as glueballs, centauros, and Higgs bosons.
- Determination of pomeron universality in conjunction with HERA results.

The understanding of strong interactions is incomplete without inclusion of soft and hard diffractive processes. The Tevatron is the ideal collider to study this physics due to the large center-of-mass energy available, and the addition of the FPD will greatly augment the physics possibilities of the DØ detector.

# 3 The FPD Layout and Acceptance

The Forward Proton Detector is a series of momentum spectrometers which make use of machine magnets along with points measured on the track of the scattered proton (or anti-proton) to calculate its momentum and scattering angle ($\theta \sim \sqrt{t}$). The points are measured using detectors located in Roman pots, which are typically stainless steel pots or containers that allow the detectors to function close to the beam. Particles traverse thin steel windows at the entrance and exit of each pot. The pots are remotely controlled and can be moved close to the beam (within a few mm) during stable beam conditions and retracted otherwise.

## 3.1 Dipole Spectrometer

Figure 8 shows the proposed location of the Roman pots that will comprise the Forward Proton Detector, where $A$ refers to the outgoing anti-proton side, $P$ the outgoing proton side, $Q$ represents the low beta quadrupole magnets, $D$ the dipole magnets, and $S$ the electrostatic separators. The dipole spectrometer consists of two Roman pot detectors ($A_{D1}$ and $A_{D2}$) located after the bending dipoles about 57 meters downstream of the interaction point on the outgoing $\overline{p}$ arm. The other Roman pots in the figure are components of the quadrupole spectrometers discussed in the next section. The dipole spectrometer pots are located inside the Tevatron ring in the horizontal plane to detect scattered anti-protons that have lost a few percent of the original beam momentum. These are the equivalent positions of the CDF pots (E-876) [35] which were added at the end of Run I. There are no known obstacles to implementing this portion of the FPD as the optics are roughly the same at CDF and DØ, and there is space available at the equivalent location near DØ. It is not possible to instrument the outgoing proton side with a dipole spectrometer without major modifications to the accelerator (not being considered).

Some of the physics topics mentioned in Sec. 2.2 are accessible to the dipole spectrometer, which for CDF had almost full acceptance for anti-protons with $|t| < 3$ GeV$^2$ and $0.05 < \xi < 0.1$ [12]. These include studies of diffractive jet production, diffractive $W$ boson production, and pomeron structure. CDF has preliminary results using their new (anti-)proton detector and sees events consistent with diffractive jet production, although there are background uncertainties due to their limited $\xi$ acceptance [12]. They also have a few diffractive $W$ boson candidate events with a track in their

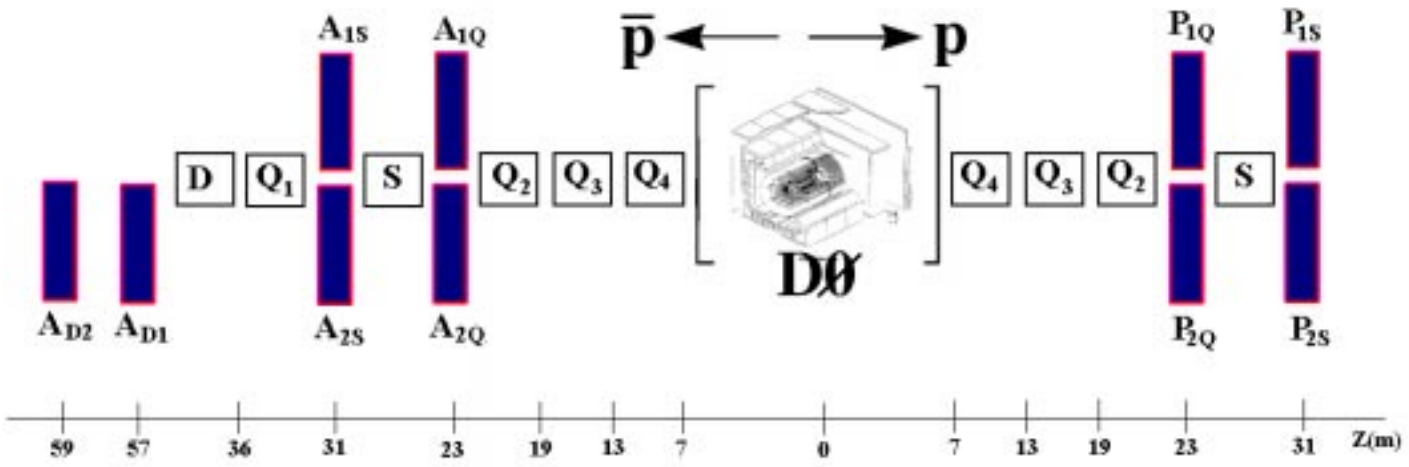


Figure 8: Placement of Roman pot detectors near the DØ interaction region. The horizontal scale shows the distance from the interaction point in meters. Each of the independent momentum spectrometers consists of two Roman pots (represented by black rectangles) in combination with the machine magnets as described in the text.

detector.

A single dipole spectrometer with acceptance characteristics similar to that of the Run I CDF spectrometer has two principal limitations: hard double pomeron exchange cannot be studied using $p$ and $\overline{p}$ tags since only the $\overline{p}$ arm is instrumented, and the acceptance is restricted to a relatively large $\xi$ region where the backgrounds from other processes are large and hard to understand.

To remove these limitations, the FPD discussed in this document is optimized to improve the acceptance and also includes quadrupole spectrometers.

### 3.2 Quadrupole Spectrometers

There is currently no space for Roman pots except for the dipole spectrometer pots $A_{D1}$ and $A_{D2}$. The instrumentation of both the outgoing proton and anti-proton arms requires modifications to the machine lattice to create

space for the detectors. The proposal here involves moving the three low beta quadrupoles on each side ($Q_4$, $Q_3$, and $Q_2$) about two-thirds of a meter closer to the interaction region, in order to create two one-third meter spaces for the Roman pot stations. Roman pots would be located at either end of the electrostatic separators, which would be moved one-third meter closer to the interaction region. Figure 9 shows a sketch of the proton-side separator with Roman pots inserted. The area within the bypass is the only "warm" section of beam pipe in reasonable proximity to the DØ detector, and is thus the obvious choice for the location of Roman pots.[3] The details of the modifications are discussed in Sec. 6.

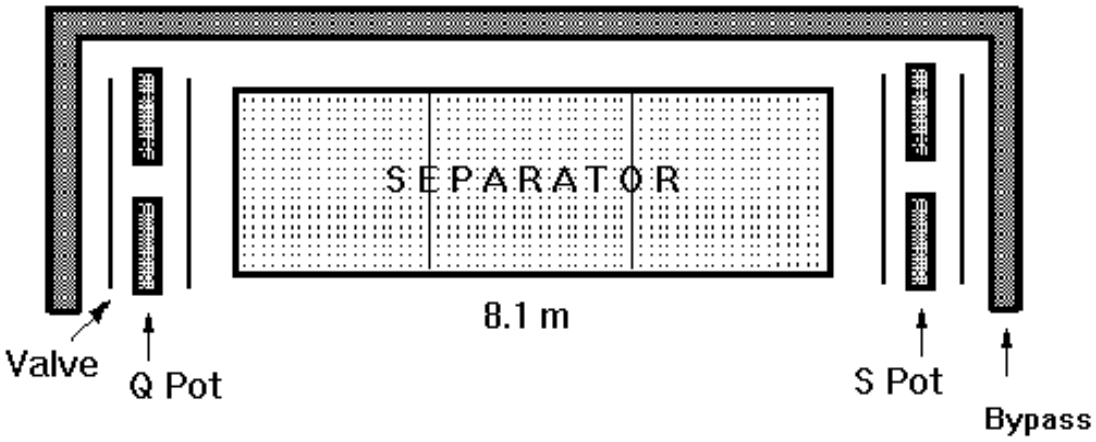


Figure 9: A sketch of the electrostatic separator on the proton side with Roman pots inserted. The pots will be isolated from the separator by a vacuum valve on either side.

The FPD thus will consist of six Roman pot stations, the aforementioned $A_D$, which has two stations, plus four stations that use the quadrupole magnets to measure the proton ($P_Q$ and $P_S$) or anti-proton ($A_Q$ and $A_S$) trajectory instead of the dipole magnets.

An ideal proton detector would be an annular detector with full $\phi$ accep-

[3] Installing Roman pots in a "cold" (super-conducting) region of the accelerator requires extensive modifications.

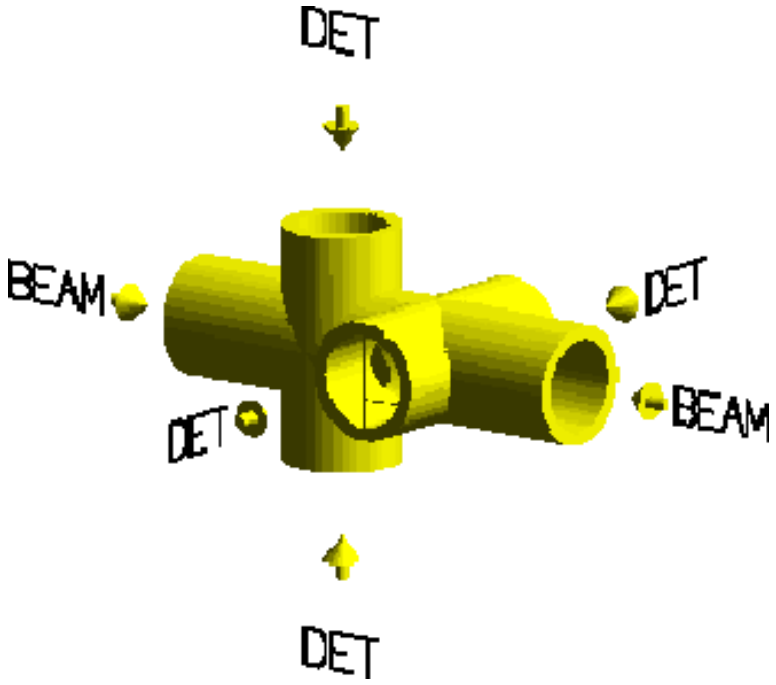


Figure 10: The "Cross" design of the beam pipe which allows Roman pots in the horizontal and vertical planes. There will be four detectors ("DET") per quadrupole station. The entire beam pipe section will only be about 12 inches long.

tance close to the beam. Since it is necessary to remove the detector during injection of the beam for stability and radiation considerations, such a design is impractical. Typically Roman pot stations have consisted of pairs of pots in either the horizontal or vertical plane, which generally provide adequate but not optimal acceptance. We are proposing a "cross" design (see Fig. 10), which maximizes the acceptance for protons and anti-protons by allowing pots in both the horizontal and vertical planes.

With this "cross" design there are eight independent quadrupole spectrometers, four on each side of the interaction region (two each in the $x$ and $y$ directions). This gives a total of 18 pots, 2 dipole pots and 16 quadrupole pots. An example of a quadrupole spectrometer is the $P_1$ spectrometer (first proton spectrometer) shown in Fig. 8, which has the pot $P_{1Q}$ located after the $Q_2$ quadrupole about 23 m from the interaction point, and $P_{1S}$ located about 31 m from $z = 0$. A proton deflected to the left of the beam axis

would be detected in this spectrometer while a proton scattered to the right would be detected in the $P_2$ spectrometer in pots $P_{2Q}$ and $P_{2S}$. There would also be $P_3$ and $P_4$ spectrometers (not shown in Fig. 8 for simplicity) for protons scattered above and below the beamline. Analogous spectrometers are located on the anti-proton side.

Although studies (discussed in Sec. 6) must be completed to show the feasibility of moving the quadrupole magnets, the implementation of this entire proposal provides a vast improvement over the dipole spectrometer alone. The gains are as follows

- Instrumenting both sides allows tagging of both protons and anti-protons and thus the unambiguous measurement of double pomeron exchange (for example, the outgoing proton could be detected in the $P_1$ spectrometer while the outgoing anti-proton could be detected in the $A_1$ spectrometer). By measuring the $x_p$ and $|t|$ of the outgoing beam particles and the products of the interaction in the central detector, the event kinematics are fully determined.

- Instrumenting both sides using quadrupoles allows the detection of elastic scattering events (for example, a $P_1$–$A_2$ combination with both particles at the beam momentum would be dominated by elastic scattering). A major concern with Roman pot detectors is alignment, and the in situ calibration afforded by elastic scattering would be invaluable. Elastic scattering events could also be used for luminosity monitoring by measuring the elastic cross section for each run.

- Diagonally opposite spectrometers can be used to reject halo background, as in-time halo tracks in one spectrometer appear as early hits in the other spectrometer (for example, a track in $P_1$ accompanied by an early time hit in $A_{2Q}$ would be a signal for a halo event).

- The combination of dipole and quadrupole spectrometers also provides many advantages. A subset of the anti-proton tracks will have hits in both the $A_2$ and the $A_D$ spectrometers. This will allow alignment of the $A_D$ spectrometer and provide an excellent means for checking efficiencies. The full $|t|$ coverage of $A_D$ will be crucial for calculating the acceptance of the quadrupole spectrometers and avoiding uncertainties in the extrapolation to $|t| = 0$, and also results in large acceptance for high mass events and double pomeron exchange (in conjunction with the proton quadrupole spectrometer).

### 3.3 Tracking Studies

To study the acceptance of the spectrometers, we used a tracking program provided by the Beams Division. [36] This program tracks particles through each element of the lattice, using the measured lengths and magnetic fields of the elements. The Run II beam energy of 1 TeV was assumed in the lattice calculations. The user provides the initial conditions of the proton ($x$, $y$, c$\Delta$t, $x$', $y$', $\Delta$p/p) and the program gives the six-vector as a function of longitudinal distance from the interaction point.

Several iterations of the acceptance studies have been performed. Initial studies used a 1 TeV version of the Run I lattice. Subsequent studies involved moving the quadrupoles to simulate the desired Run II conditions, and then switching to the proposed Run II dispersion-free lattice [37]. The final studies shown here were done using a modified version of the dispersion-free lattice, as moving the quadrupoles necessitates a few percent change in the gradients in order to properly retune the Tevatron [37].

The acceptance is critically dependent on the distance of the detector from the beam axis, which depends on the beam width ($\sigma$).[4] Table 1, which is extracted from a detailed study of the background from accelerator losses [38], shows the beta function and corresponding $8\sigma$ beam widths at the proposed Roman pot locations (dipole pots are only useful in the horizontal plane). Normalized emittances of 3 mm·mrad for protons and 2.2 mm·mrad for anti-protons were assumed, but the larger $8\sigma$ proton widths were used in Table 1. Figure 11 shows a sketch of a pair of pots located at $8\sigma$ from the proton beam for the case of no separation of beams (both beams have the same axis), which is the situation for the quadrupole spectrometers. The pot displacement is clearly limited by the wider proton beam, not the $\overline{p}$ beam for which $8\sigma_{\overline{p}} \approx 7\sigma_p$.

The $8\sigma$ beam width over the entire distance from the interaction point through the pot locations is shown in Fig. 12. Roman pots placed at $8\sigma$ from the beam could detect scattered $p$'s and $\overline{p}$'s with displacements larger than than this. A comparison of the $Q$ and $S$ rows of the table for $p$'s and $\overline{p}$'s reveals that for this lattice the horizontal plane for protons is equivalent to the vertical plane for $\overline{p}$'s and vice versa. This point will be discussed further in Sec. 3.3.2 and leads to the "cross" design mentioned earlier. Figure 13

[4] The horizontal beam size is given by $\sigma_x^2 = (\beta_x \epsilon)/(\beta\gamma) + (\eta\sigma_{\rm p}/{\rm p}_0)^2$ where $\beta_x$ is the horizontal beta function, $\epsilon$ is the normalized emittance, $\beta\gamma \approx 1066$ at 1 TeV, and $\sigma_{\rm p}/{\rm p}_0$ is the momentum spread. For the dispersion-free lattice the dispersion parameter $\eta$ is zero and the second term can be ignored.

shows a cross section sketch of the four $P_Q$ pots inserted at $8\sigma$ from the beam axis.

| Roman Pot Station | $\beta_x$(m) | $\beta_y$(m) | $8\sigma_x$(mm) | $8\sigma_y$(mm) |
|---|---|---|---|---|
| $A_{D1}$ | 177 | - | 5.64 | - |
| $A_{D2}$ | 140 | - | 5.01 | - |
| $A_Q$ | 1160 | 254 | 14.5 | 6.77 |
| $A_S$ | 949 | 118 | 13.1 | 4.61 |
| $P_Q$ | 255 | 1155 | 6.78 | 14.4 |
| $P_S$ | 121 | 941 | 4.66 | 13.0 |

Table 1: $\beta$-functions and $8\sigma$ positions at the Roman pot locations.

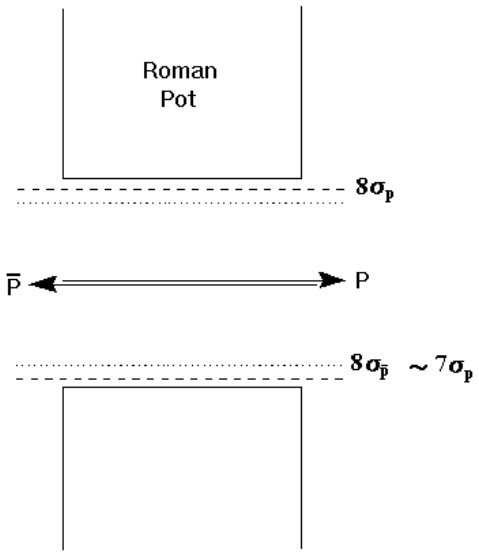


Figure 11: The $8\sigma$ proton and anti-proton beam widths are shown for the case of no beam separation. The closest approach of the pots is limited by the proton beam width.

The tracking program is used to map out the acceptance in $|t|$ and $\phi$. For a track to be accepted, it must remain within the beam pipe (inner radius of 35 mm) and within the separator aperture (25 mm). It must also pass through the active area of the detector in both pots, which is assumed to cover $x_{min} < x < x_{min} + 20$ mm and $-10 < y < 10$ mm for horizontal

pots ($x$ and $y$ are interchanged for vertical pots). The $x_{min}$ ($y_{min}$) values are obtained from the $8\sigma_x$ ($8\sigma_y$) column in Table 1.

An example of the results of the tracking program is given in Fig. 14, which shows trajectories of protons with $\Delta$p/p $= -0.02$ (corresponding to $x_p = 0.98$). Figure 14(a) shows the displacement in $x$ with $y = 0$ as a function of the distance in $z$ from the interaction point. The shaded region shows the range of momentum transfers accepted by quadrupole spectrometer pots placed at $8\sigma$ beam widths from the beam axis. Figure 14(b) shows the displacement in $y$ with $x = 0$. The minimum trajectory is typically limited by the displacement of the $S$ pot, while the maximum trajectory is limited by the beam pipe in Fig. 14(a) and the separator aperture in Fig. 14(b). For reference, momentum transfers of $|t| = 0.5$ and $|t| = 3.5$ GeV$^2$ correspond to angles of 0.7 and 1.9 mrad, respectively. Details of the acceptance are discussed later in this section.

The acceptance is maximized by minimizing the distance between the detectors and the beam axis. This distance is limited primarily by the halo rates which increase as the pots are inserted closer to the beam.[5] Using an initial intensity of $10^{13}$ protons per bunch, we have determined that the beam halo rates for an $8\sigma$ pot location are on the order of $10^5$ protons/second in the quadrupole pots [38], and a factor of two higher in the dipole pots. The halos rates decrease by about a factor of three at $9\sigma$ and quickly decrease with larger pot displacements. There is some dependence on the assumptions and exact collimation scheme, which has not been tuned to minimize the rates at the pot positions. With a crossing rate of 1.7 MHz, a 100 kHz halo rate implies that one out of every 10–20 crossings will have a hit from halo. Details of the effect of halo backgrounds are given in Sec 5.3.2, and this magnitude of the halo background is determined to be acceptable. The real rates will have to be measured and the exact pot displacements will then be determined. The current studies indicate that a reasonable pot location is between 8 and $9\sigma$ for quadrupole pots and $10\sigma$ for dipole pots.

[5] Background to the DØ detector caused by scattering off the pots is another concern, and is discussed in Sec.5.1.

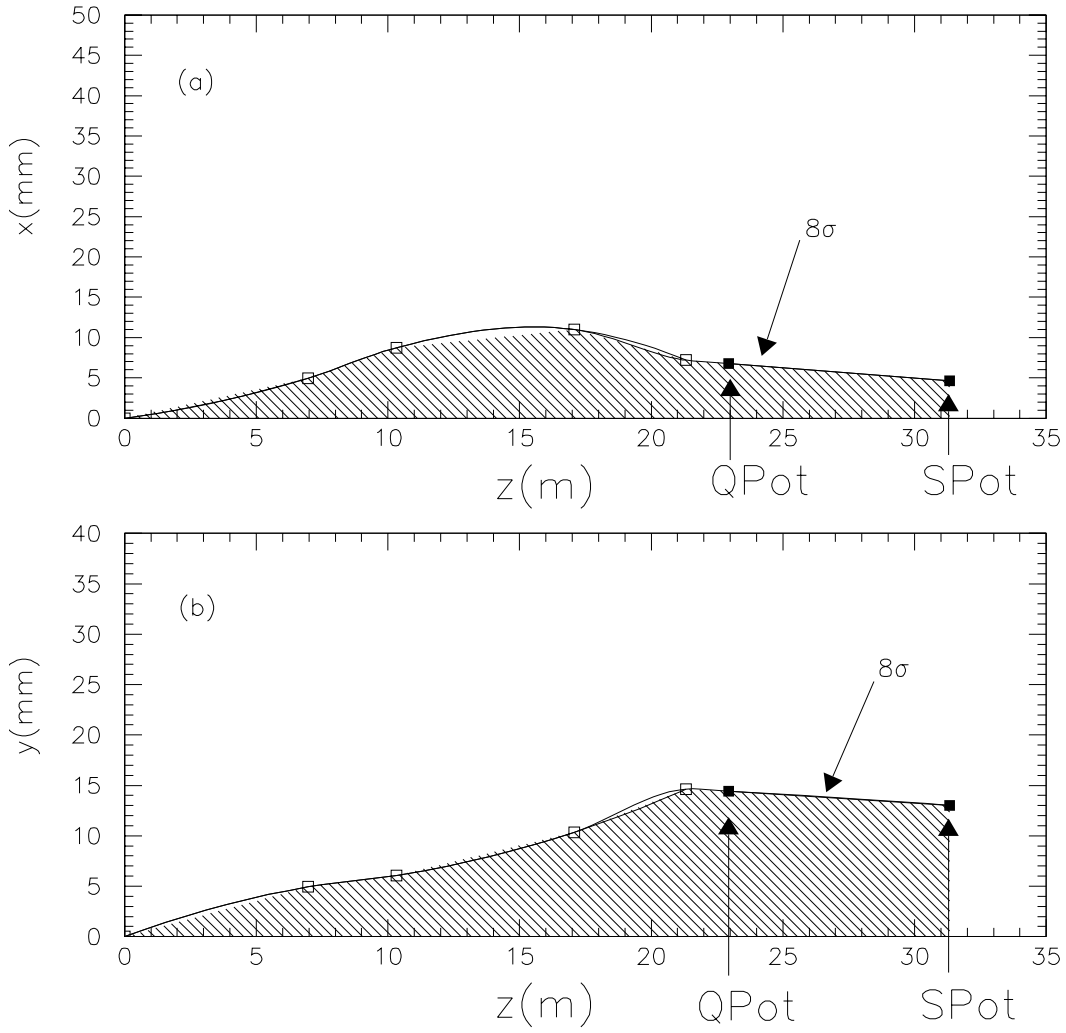


Figure 12: The $8\sigma$ proton beam envelopes are shown for (a) the horizontal plane and (b) the vertical plane as a function of distance from the interaction point. The pot locations are marked in the figure.

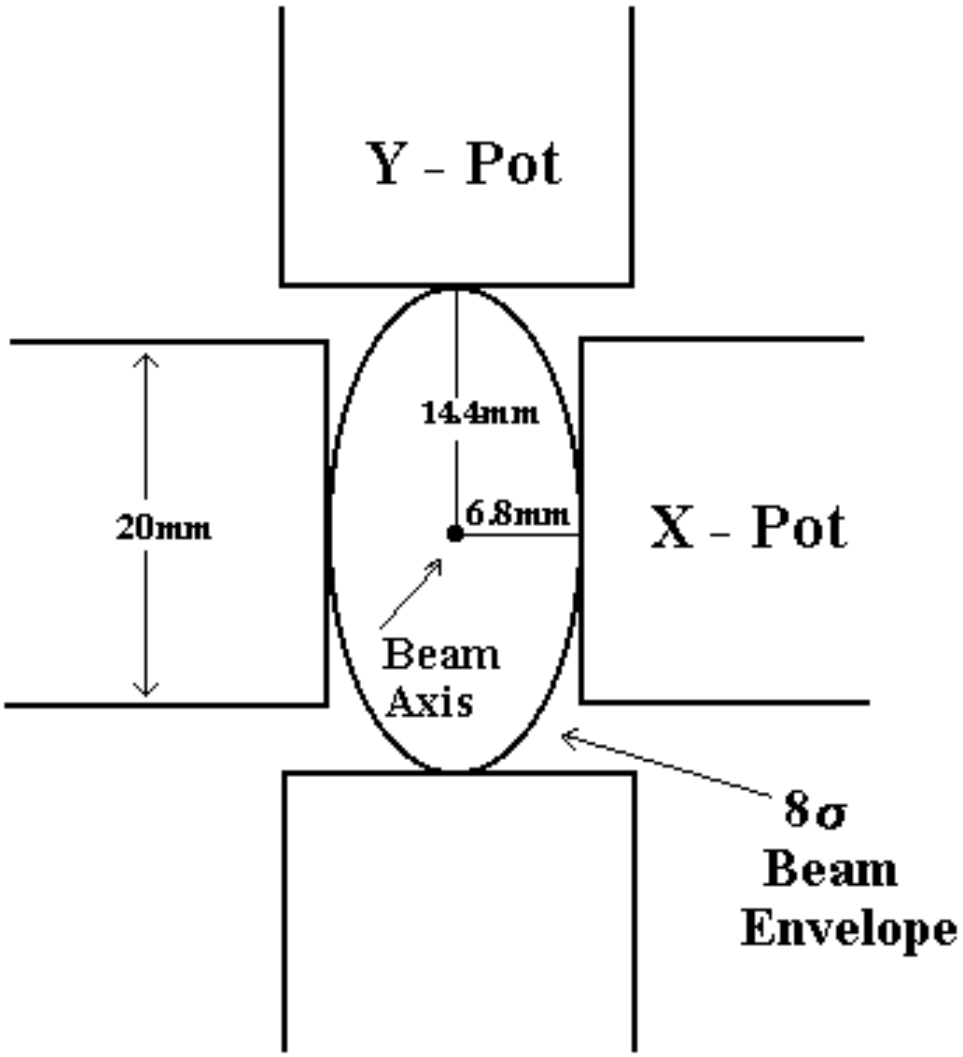


Figure 13: A cross section view of the four $P_Q$ pots (only the active area is shown). The pots are inserted at $8\sigma$ from the beam axis, and are thus tangent to the $8\sigma$ proton beam profile.

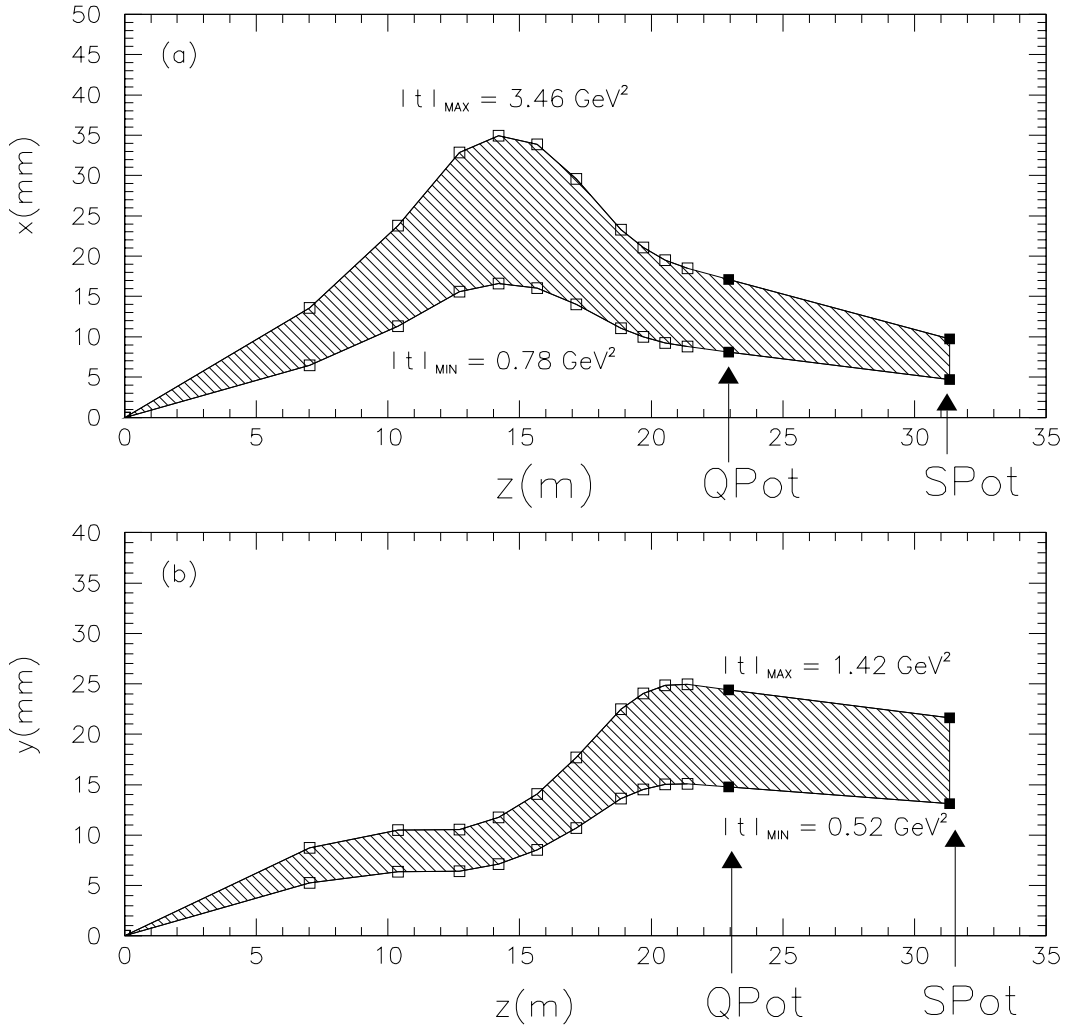


Figure 14: The trajectory of a proton with $x_p = 0.98$ is shown for the range of momentum transfer accepted by pots at a displacement of $8\sigma$ beam widths from the beam axis. (a) shows the $x$ displacement from the beam axis for $y = 0$ versus the distance in $z$ from the interaction point (b) shows the $y$ displacement for $x$=0. Larger values for $|t|_{MAX}$ can be obtained when the requirement that the scattering take place in only one plane is relaxed.

### 3.3.1 Dipole Spectrometer Acceptance

The nominal $10\sigma$ values for dipole spectrometer pot locations are obtained by scaling the $8\sigma$ values from Table 1 and give an $x_{min}$ of 7.0 mm and 6.3 mm, for $A_{D1}$ and $A_{D2}$, respectively. An anti-proton is considered to be accepted by the dipole spectrometer if it passes through the active area of both detectors while remaining within the limiting aperture of the beam pipe throughout its entire trajectory. The acceptance is determined as a function of the initial conditions of the anti-proton ($\phi$, $|t|$, and $\xi$).

The geometric ($\phi$) acceptance of the dipole spectrometer is shown in bins of $\xi$ and $|t|$ in Fig. 15. The size of the boxes are proportional to the geometric acceptance with the largest boxes representing 100% acceptance. The acceptance is especially good for $0 < |t| < 0.5$ GeV$^2$ and high $\xi$ ($\xi > 0.02$). At low $|t|$ and $\xi$ the particle is not deflected enough to enter the pots, while at high $|t|$ and $\xi$ the particle is deflected too much and scatters off the beam pipe.

We calculate the total acceptance (or cross section times acceptance, $\sigma \cdot A$) by integrating over the $\phi$ and $|t|$ values accepted by the pots. We include the $|t|$ dependence using the relation $d\sigma/dt \sim e^{-b|t|}$, where $b = 4.2 - 0.5ln(\xi)$ from Ref. [21]. This expression is valid for single diffractive and most likely double pomeron events, but for elastic events $b \approx 17$ [22]. The total acceptance is dominated by the $|t|$ acceptance, since the cross section falls so steeply with $|t|$.

The solid line in Fig. 16 shows the total acceptance for diffractive events for $10\sigma$ pot positions. For comparison, the acceptance for pot positions of $8\sigma$ (dashed line) and $13\sigma$ (dotted line) are also shown. The acceptance increases rapidly with increasing $\xi$ for all pot displacements. Even for $13\sigma$ there is still acceptance at low $\xi$. The $10\sigma$ acceptance for several $\xi$ and $M_X$ values is summarized in Table 2. Although we are only focussing on the acceptance for $\xi < 0.05$, the dipole spectrometer retains $> 50\%$ acceptance up to $\xi \approx 0.07$.

| | Total Acceptance (%) vs. $\xi$ and $M_X$ (GeV/$c^2$) | | | | |
|---|---|---|---|---|---|
| Dipole | $\xi = 0.002$ | $\xi = 0.01$ | $\xi = 0.02$ | $\xi = 0.03$ | $\xi = 0.05$ |
| Spectrometer | $M_X = 90$ | $M_X = 200$ | $M_X = 280$ | $M_X = 350$ | $M_X = 450$ |
| | 3 | 12 | 35 | 74 | 96 |

Table 2: Integrated total acceptance (in percent) for anti-protons using a $10\sigma$ Roman pot displacement in the horizontal plane versus $\xi$ and $M_X$.

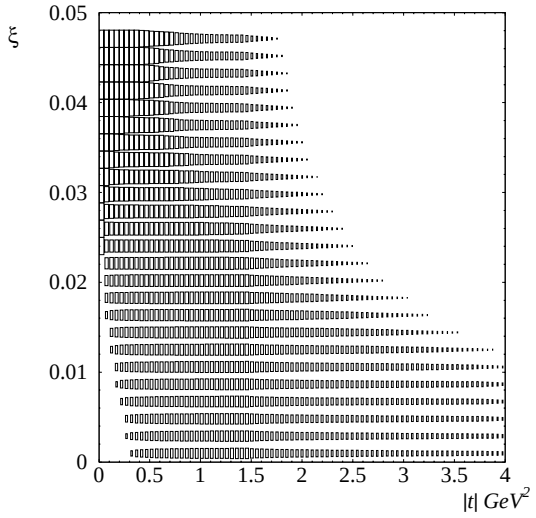


Figure 15: The geometric acceptance in bins of $\xi$ and $|t|$ for the dipole spectrometer with the detectors at the nominal $10\sigma$ displacements. The acceptance in each bin is proportional to the size of the box, with the largest box representing 100% acceptance.

It was mentioned earlier that CDF had little acceptance for $\xi < 0.05$. This was due to several factors [39]:

- One loss of acceptance was due to 1.5 mm of dead area between the bottom of their pots and the active area of their detector. The dead area was due to the thickness of the bottom of the pot as well as the frame holding the fibers.
- The beams were separated by a few millimeters at the CDF pot locations, with the proton beam located between the $\overline{p}$ beam and the pots, thus limiting the point of closest approach of the pots to the $\overline{p}$ beam.
- Since the CDF pots were installed late in Run I, their procedure for installing the pots as close to the beam as possible was not optimized.

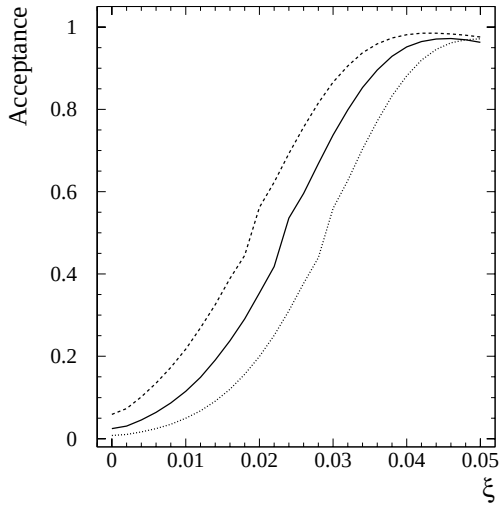


Figure 16: The total acceptance as a function of $\xi$ for the nominal $10\sigma$ pot displacements (solid line). The acceptance is integrated over $|t|$ and $\phi$ and assumes a single diffractive $|t|$ dependence as discussed in the text. For reference, the acceptance for $8\sigma$ (dashed line) and $13\sigma$ (dotted line) are also shown.

Running a few millimeters closer to the beam than their nominal position increased both signal and background rates, but lack of time prevented a full study so a conservative (retracted) position was chosen.

- They did actually have a few percent acceptance for $\xi \approx 0.03$, but due to the limited running period, have little data for $\xi < 0.05$.

From our studies each extra millimeter corresponds to $\delta\xi_{MIN} \approx 0.004$, thus the CDF detector location (about 13 mm from the beam), would give a $\xi_{MIN} \approx 0.03$ and near full acceptance for $\xi = 0.05$, which is consistent with their results (the Run I and Run II lattices are not identical and the beam energy is different).

The situation for the DØ dipole spectrometer will be much improved. The design we are considering for our pots, discussed in Sec. 4.1 should result in a dead area on the order of 100 $\mu$m, instead of a few millimeters.

The separation of the beams is more advantageous at the DØ location, with the $\overline{p}$ beam located 0.3 mm closer to the pots than the proton beam [40]. We will be preparing for a long run and will have adequate time to study the halo rates in order to minimize the pot displacement. The long running period will allow us to obtain large data samples even if the acceptance were significantly less than 1%. We consequently expect to have acceptance to $\xi$ near zero, as shown in Fig. 16.

To better understand the acceptance, it is instructive to study Fig. 17, which shows the horizontal and vertical displacements at the $A_{D1}$ and $A_{D2}$ pot locations for scattered $\overline{p}$'s with $\xi = 0.02$ (top plots) and $\xi = 0.05$ (bottom plots). The ellipses are contours of constant $|t|$ ranging from 0.5 GeV$^2$ for the inner-most ellipse to 2.0 GeV$^2$ for the outer-most ellipse. The ellipses are displaced in the negative $x$ direction due to the bending into the Tevatron ring of particles with less than the beam momentum. Comparing the ellipses for $\xi = 0.05$ and $\xi = 0.02$ shows that this deflection is larger for higher $\xi$ (lower $\overline{p}$ momentum) as expected. The dashed bracket (superimposed on $A_{D2}$ locations) represents a detector at the proposed $10\sigma$ displacement. It clearly intercepts a large portion of the ellipses, including the critical low $|t|$ values. A detector with a displacement of 13 mm shown by the dotted bracket on the $A_{D1}$ plots will clearly have much worse acceptance.

### 3.3.2 Quadrupole Spectrometer Acceptance

Quadrupole spectrometers are fundamentally different from dipole spectrometers, in that they require a minimum angle or $|t|$ to accept scattered protons rather than a minimum momentum loss. This has the obvious advantage of fairly uniform acceptance down to $\xi = 0$, but the total acceptance $(\sigma \cdot A)$ is typically only a few percent due to the steeply falling $|t|$ distribution of diffraction.

Figure 18 shows the minimum $|t|$ value accepted by proton and antiproton spectrometers in the horizontal plane as a function of $\xi$ for $8\sigma$ pot displacements. Note that $|t|_{MIN} \approx 0.5$ GeV$^2$ for both sides at low $\xi$, but while the $\overline{p}$ side (solid curve) has little $\xi$ dependence, $|t|_{MIN}$ increases quickly with $\xi$ for the proton side (dashed curve).[6] The minimum $|t|$ value is determined by the displacement of the second pot of the spectrometer ($A_S$ or $P_S$), while the maximum value of about 3.9 GeV$^2$ is limited by the aperture at the start of the separators. The $|t|$ acceptance is virtually identical

[6] For UA8 $|t|_{MIN}$ was about 0.8 GeV$^2$ [6].

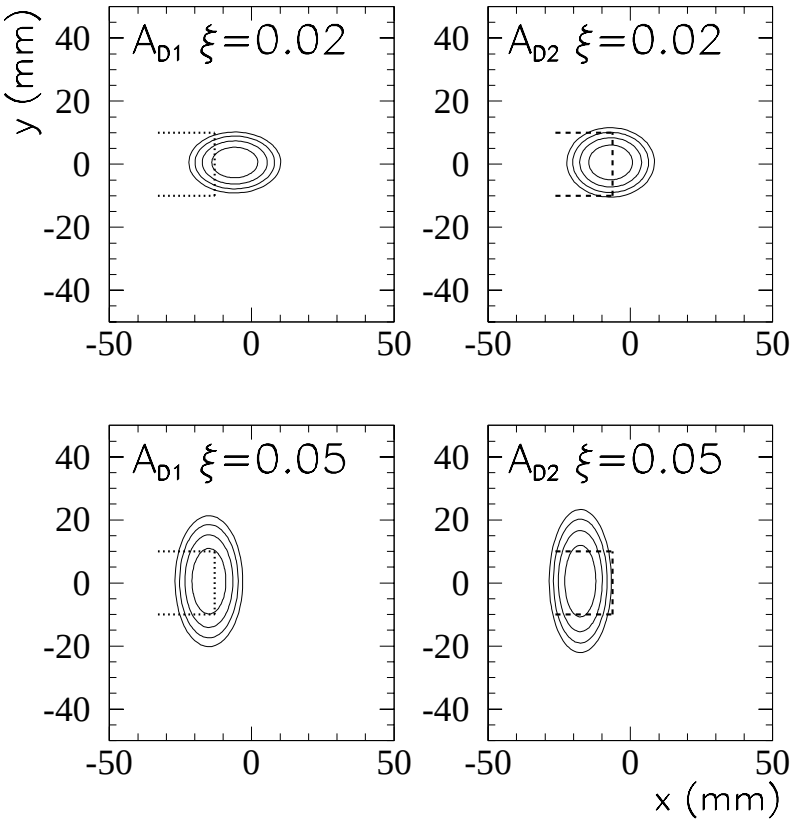


Figure 17: The $x$ and $y$ displacements at the $A_{D1}$ (left plots) and $A_{D2}$ (right plots) pot locations are shown as contours of constant $|t|$, ranging from 0.5–2.0 GeV$^2$ (smaller $|t|$ gives smaller displacement) for $\xi = 0.02$ (top plots) and 0.05 (bottom plots). The dashed brackets show a pot displacement of 6.3 mm ($10\sigma$), while the dotted brackets show a pot displacement of 13 mm (CDF Run I position).

for pots in the vertical plane, except that proton $y$ pots have the superior acceptance.

This asymmetric behaviour can be explained by the different $\beta$ functions discussed in Sec. 3.3, which arise from a different arrangement of the low beta quadrupole triplets (the proton side has DFD and $\overline{p}$ side has FDF, where F is focusing and D is defocusing). The manner in which the asymmetry in

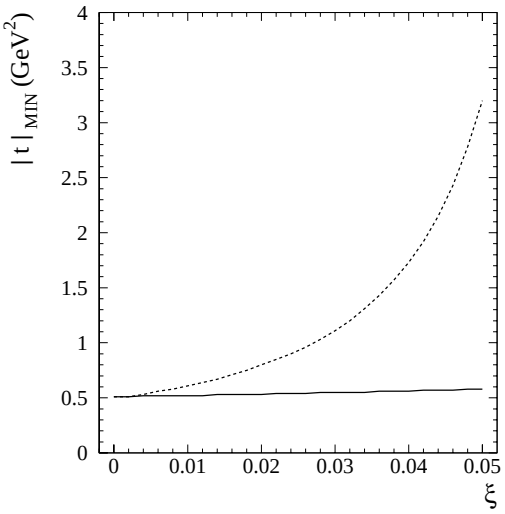


Figure 18: The minimum $|t|$ value accepted by anti-proton (solid curve) and proton (dashed curve) spectrometers in the horizontal plane versus $\xi$ for $8\sigma$ pot displacements. For pots in the vertical plane, the definition of the curves is reversed.

the optics affects the acceptance is demonstrated by Fig. 19. This figure, similar in style to Fig. 17 for the dipole spectrometer, shows the horizontal and vertical displacements at the $S$ pot location for scattered $\overline{p}$'s (top plots) and $p$'s (bottom plots). The ellipses are contours of constant $|t|$ ranging from 0.5 GeV$^2$ for the inner-most ellipse to 2.0 GeV$^2$ for the outer-most ellipse. Unlike the dipole case, the ellipses are centered at $(x = 0, y = 0)$ independent of $\xi$. Note the 90° rotation of the ellipses for $p$ pots relative to $\overline{p}$ pots. By comparing the curves for $\xi = 0.02$ (left plots) and $\xi = 0.05$ (right plots), it is easy to see that the acceptance for horizontal (dashed brackets) $\overline{p}$ pots is relatively insensitive to changes in $\xi$. For horizontal $p$ pots, however, the contours are very close together and the acceptance vanishes with increasing $\xi$ as the ellipses become more squashed. For vertical pots (dotted brackets) the situation is reversed, and the acceptance is more favorable for protons. The $Q$ pots exhibit similar behaviour, but only the $S$ pots are shown here since they control the acceptance.

Placing pots in both the horizontal and vertical planes will thus give us

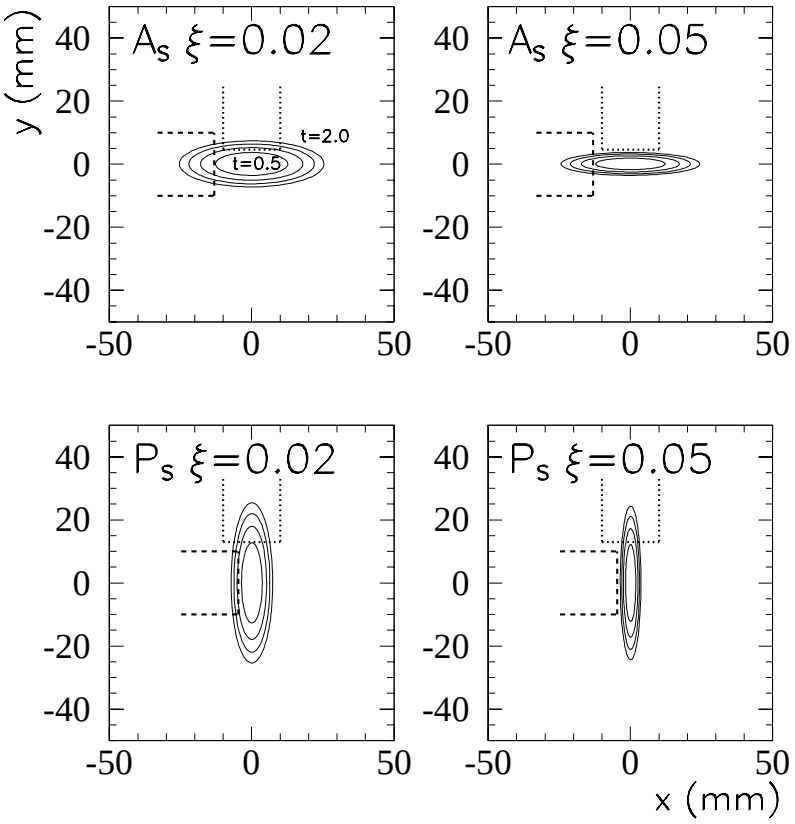


Figure 19: The $x$ and $y$ displacements at $S$ pot position are shown as contours of constant $|t|$, ranging from 0.5–2.0 GeV$^2$ (smaller $|t|$ gives smaller displacement) for $\xi = 0.02$ and 0.05. The ellipses are rotated by 90° as discussed in the text. The dashed (dotted) brackets show horizontal (vertical) pots at an $8\sigma$ displacement.

equal and stable acceptance for protons and anti-protons from the quadrupole spectrometers. Figure 20 shows the geometric ($\phi$) acceptance for horizontal and vertical pots in bins of $\xi$ and $|t|$ with the size of the boxes again proportional to the geometric acceptance (the maximum acceptance in this case is about 83%). There is no acceptance for $|t| < 0.5$ GeV$^2$ as discussed earlier, but the intermediate and high $|t|$ geometric acceptance for the quadrupole spectrometers is seen to be superior to the dipole spectrometer.

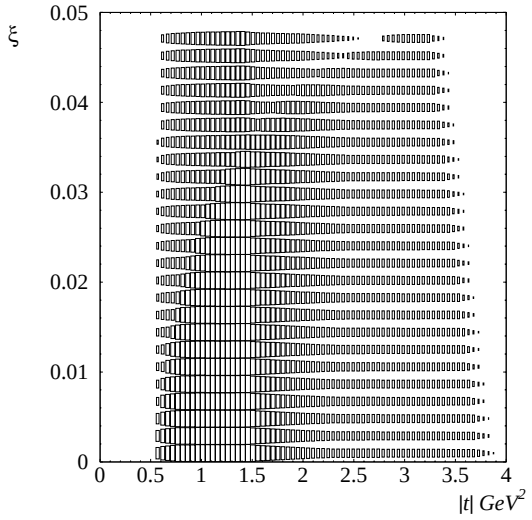


Figure 20: The geometric acceptance in bins of $\xi$ and $|t|$ for the quadrupole spectrometer with the detectors at the nominal $8\sigma$ displacements. The acceptance in each bin is proportional to the size of the box, with the largest box representing 83% acceptance.

The $8\sigma$ total acceptance $(\sigma \cdot A)$ is obtained by integrating over $|t|$ and $\phi$ and ranges from 1.2 to 1.6% for $\xi < 0.05$ as shown in Table 3. There is also reasonable acceptance up to $\xi = 0.1$ (0.9%). The acceptance in general does not depend strongly on the width of the active area of the detector, as the bulk of the acceptance is in the center of the detector. Doubling the width from 2 to 4 cm only increases the overall acceptance by a few percent of its nominal value, since this only improves the acceptance for very rare high $|t|$ events, and decreasing the width from 2 to 1.5 cm also has little effect.

As mentioned earlier, the total acceptance is quite sensitive to pot position, and we expect to place the quadrupole spectrometer pots between 8 and $9\sigma$. Figure 21 shows the acceptance for protons (or $\overline{p}$'s) with $\xi = 0.02$

| Quadrupole Spectrometers | Total Acceptance (%) vs. $\xi$ and $M_X$ (GeV/$c^2$) | | | | |
|---|---|---|---|---|---|
| | $\xi = 0.002$ $M_X = 90$ | $\xi = 0.01$ $M_X = 200$ | $\xi = 0.02$ $M_X = 280$ | $\xi = 0.03$ $M_X = 350$ | $\xi = 0.05$ $M_X = 450$ |
| | 1.4 | 1.6 | 1.4 | 1.3 | 1.2 |

Table 3: Integrated acceptance (in percent) for protons or anti-protons using $8\sigma$ Roman pot locations in both the horizontal and vertical planes vs. $\xi$ and $M_X$.

as a function of pot displacement in units of $\sigma$. The acceptance is seen to decrease by about a factor of three for each additional $\sigma$ unit: the nominal $8\sigma$ acceptance of 1.3% increases to 3.6% for $7\sigma$, and decreases to 0.5% for $9\sigma$.

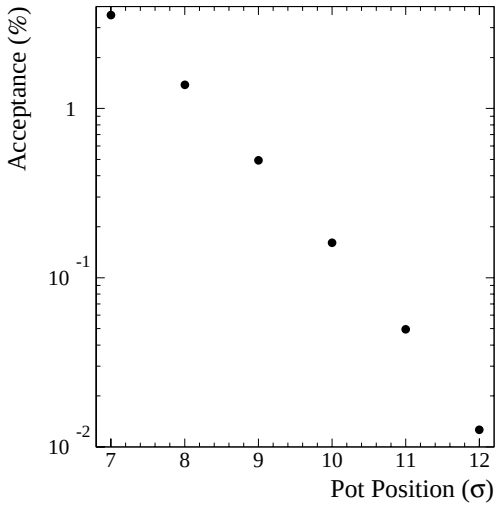


Figure 21: Acceptance for scattered protons (or $\overline{p}$'s) as a function of the pot position in units of $\sigma$.

Other factors going into the exact acceptance include beam crossing angles (next section), the final details of the lattice (which could affect the acceptance by roughly a factor of two in either direction), and the emittance (which would affect the acceptance if it is much smaller or larger than the expected value).

### 3.3.3 Crossing Angle

Run II at the Tevatron will begin with 36 bunches and eventually be upgraded to about 100 bunches (132 nsec running). With 36 bunches there are twelve potential collision points around the Tevatron ring. The use of electrostatic separators allows the beams to collide with a zero crossing angle at the DØ and CDF interaction points, but have a $5\sigma$ separation at the other parasitic crossings. With 132 nsec running, however, it will no longer be possible to avoid the first parasitic crossing without the introduction of a crossing angle to separate the beams within the low beta quadrupoles. A preliminary study of 132 nsec running [40, 41] indicates that a crossing angle of about 140 $\mu$rad will provide a $3\sigma$ separation of the beams at the first parasitic crossing (roughly the quadrupole spectrometer Roman pot locations) and $6.5\sigma$ at the other undesirable crossing points.

The dipole spectrometer situation is improved by the addition of the crossing angle which will result in a 2.3 mm separation of the $p$ and $\overline{p}$ beams [40], with the proton beam located farthest away from the pots. It should be possible to move the pots slightly closer to the $\overline{p}$ beam in this case, due to the smaller $\overline{p}$ beam width.

Figure 22 shows the effect of a crossing angle on the quadrupole spectrometers. There is no longer symmetric acceptance in the plane of the crossing angle. The current scenario assumes that the crossing angle is split among the $x$ and $y$ directions, and results in a $3\sigma$ separation of the beam in each plane [40]. For the case of proton side pots, the effect of the separated beams is that one spectrometer is still $8\sigma$ from the proton beam but the other side now has the $\overline{p}$ beam in the way and can only be inserted to $10\sigma$ ($3\sigma$ from the beam separation and $7\sigma$ from the effective width of the $\overline{p}$ beam). The overall acceptance for this side will thus drop by almost a factor of two, since $10\sigma$ pot displacements give an acceptance almost 10 times smaller than $8\sigma$. For the anti-proton side pots, the acceptance is actually increased by about 50% as for one spectrometer the pots can be lowered to $7\sigma$ from the $\overline{p}$ beam (which gives an increase of about a factor of 3), while the other side spectrometer will be at $11\sigma$ and can be ignored. The addition of a crossing angle, although not desirable from complexity and symmetry arguments, does not significantly affect the overall acceptance and does not compromise the goals of the FPD.

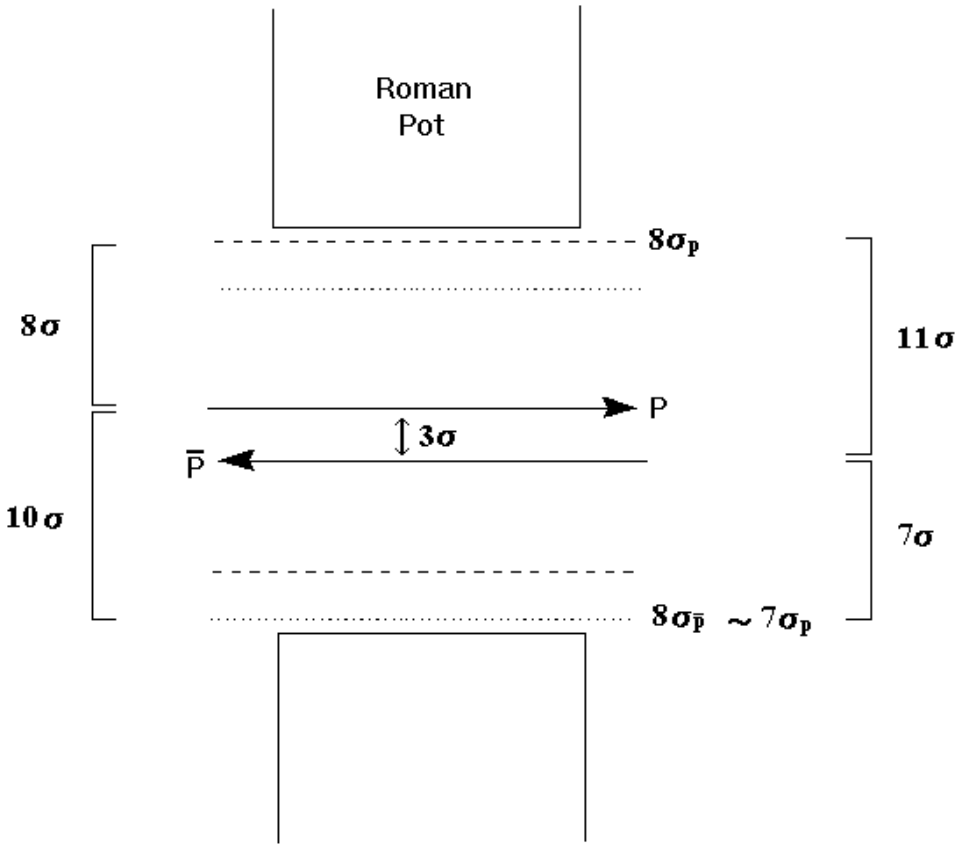


Figure 22: The pot locations in a crossing angle scenario are shown. The proton and anti-proton beams are separated by $3\sigma$ resulting in effective pot positions of 8 and $10\sigma$ for $p$ pots and 7 and $11\sigma$ for $\overline{p}$ pots.

### 3.3.4 Resolution

The transport matrix obtained from the tracking program can be used to derive the resolution expected from the spectrometers. The horizontal transfer from the vertex to the $P_Q$ ($A_Q$) Roman pot is given by Eq. 1.

$$\begin{pmatrix} m11 & m12 & m13 \\ m21 & m22 & m23 \\ 0 & 0 & 1 \end{pmatrix} \cdot \begin{pmatrix} 0 \\ x'_o \\ \Delta\mathrm{p/p} \end{pmatrix} = \begin{pmatrix} x_Q \\ x'_Q \\ \Delta\mathrm{p/p} \end{pmatrix} \tag{1}$$

where $x_Q$ is the horizontal position of the particle in the $Q$ pots, $x'_Q$ is the angle from the $Q$ to $S$ pots, and $x'_o$ is the initial angle from the interaction point (IP).

The particle's initial conditions at the IP ($x'_o$ and $\Delta$p/p) are reconstructed from the detector readings ($x_Q$ and $x'_Q$) through the equations:

$$\Delta\mathrm{p/p} = \frac{\mathrm{x'_Q - x_Q \cdot m22/m12}}{\mathrm{m23 - m22 \cdot m13/m12}} \tag{2}$$

$$x'_o = \frac{x_Q - m13 \cdot \Delta\mathrm{p/p}}{m12} \tag{3}$$

$$x'_o = \frac{x'_Q - x_Q \cdot m23/m13}{m22 - m12 \cdot m23/m13} \tag{4}$$

The transfer matrix parameters from the IP to the $P_Q(A_Q)$ pots are given below:

$m12 = 9.47(20.2)$
$m13 = 23.5(9.02)$
$m22 = -0.345(-0.220)$
$m23 = 3.45(1.57)$
$x_Q = [\mathrm{mm}], \quad x'_Q = [\mathrm{mrad}]$

The detector resolutions can be calculated from these equations using the substitutions $\xi = -\Delta\mathrm{p/p}$ and $x'_o = \theta = \sqrt{t}/(\mathrm{p_{beam}} \cdot \sqrt{x_p})$. The following equations for the resolution are obtained:

$$\delta\xi = 0.008\delta x_Q \tag{5}$$

$$\delta t = 0.12\sqrt{t} \cdot \delta x_Q \tag{6}$$

The value of $\delta x_Q$ depends on the point resolution of the detector and multiple scattering, which are estimated to be about 0.1 mm and 0.04 mm,

respectively, for the detector discussed in Sec. 4.2.1. It is also sensitive to the uncertainty in the beam position at the $P_Q$ location. The average beam position can be measured very well using elastic events, and deviations from this position are expected to be about 0.1 mm [38]. Adding these resolutions in quadrature gives $\delta x_Q \approx 0.15$ mm. This yields estimated resolutions of $\delta\xi = 0.0012$ and $\delta t = 0.018\sqrt{t}$. In practice, the $|t|$ resolution is dominated by the 0.06 mrad angular dispersion of the beam, which corresponds to $\delta t = 0.12\sqrt{t}$. These resolutions compare well with the expected dipole spectrometer resolution of $\delta\xi = 0.002$ and $\delta t = 0.1\sqrt{t}$ [35].

### 3.3.5 Acceptance Summary

Tracking studies show that with reasonable assumptions about Run II conditions, the Forward Proton Detector will have quite good acceptance for detecting scattered protons and anti-protons. The dipole spectrometer has excellent acceptance for anti-protons, especially at low $|t|$ and high $\xi$. The addition of quadrupole spectrometers allows the tagging of protons, and thus double pomeron and elastic events, as well as generally improving the intermediate and high $|t|$ acceptance. Our design with spectrometers in both the horizontal and vertical planes makes this acceptance very robust, and insulates us against accelerator uncertainties. Although the $\overline{p}$ quadrupole pots have inferior total acceptance to the dipole pots, they improve the $|t|$ coverage, are crucial for elastics and halo rejection, and will allow the calibration of the dipole spectrometer. The quadrupole total acceptance is quite stable for both protons and anti-protons with $\xi$ at the 1–2% level, with a $|t|_{MIN} \approx 0.5$ GeV$^2$ and $|t|_{MAX}$ ranging from about 2.5 GeV$^2$ at low $\xi$ to 3.9 GeV$^2$ at high $\xi$. The dipole acceptance for $\overline{p}$'s increases sharply with $\xi$ from about 2% at low $\xi$ to near 100% at high $\xi$. The minimum dipole $|t|$ varies from about 0.3 to 0 GeV$^2$ for $0 < \xi < 0.05$ (with acceptance to $|t| \approx 0$ for $\xi > 0.02$), while the maximum $|t|$ ranges from 4.1 to 1.8 GeV$^2$. A summary of the spectrometer acceptances are given in Table 4.

| Spectrometer | $\|t\|_{MIN}$ | $\|t\|_{MAX}$ | $\xi_{MIN}$ | $\xi_{MAX}$ | Acceptance |
|---|---|---|---|---|---|
| Dipole ($\overline{p}$) | 0.0 GeV$^2$ | 4.1 GeV$^2$ | 0.0 | $> 0.05$ | 2–96% |
| Quadrupole ($p$ or $\overline{p}$) | 0.5 GeV$^2$ | 3.9 GeV$^2$ | 0.0 | $> 0.05$ | 1–2% |

Table 4: Properties of dipole and quadrupole spectrometers.

# 4 Hardware

## 4.1 Roman Pots

As discussed earlier, the Roman pots are the vessels that house the detectors. There are nine independent spectrometers each consisting of two Roman pots for a total of 18 pots. There are four stations with four pots each that comprise the quadrupole spectrometers and two single pots for the dipole spectrometer. This configuration results in the optimal acceptance as discussed in the previous section.

Figure 23 shows a front view and a side view of the beam pipe section including a pair of Roman pots. Each pot is a small steel box that completely encases the scintillation fiber detector (described in the next section) and keeps it isolated from the machine vacuum, although the pot itself remains inside the machine vacuum. The dimensions are labelled on the figure and show that the pot is very compact, with a length of only 3.8 cm along the beamline, a height of 13 cm, and a width of 7 cm. The width and height are determined by the bending radius of the fibers. The pot will be fully retracted in the bay area for beam injection, and can be moved into the beam pipe at a position close to the beam for normal running. A small diameter bellows surrounds the cylindrical chimney and supports the structure. The chimney is used to route the fibers to the phototubes.

The Roman pot is composed of 2 mm thick steel except for a thin window which brackets the active area of the detector traversed by the scattered protons. The window is composed of a 50 $\mu$m stainless steel foil in order to reduce multiple scattering. Once the detector is placed inside the box, a steel lid with a cylindrical chimney is welded to the top of the box. A low viscosity epoxy will be injected through the chimney in order to fill the remaining space on either side of the detectors, thus creating a solid one-piece detector. The box design produces the smallest possible pot, reducing the space needed in the beam pipe region. This allow us to have pots in both the $x$ and $y$ planes in order to maximize the acceptance as discussed in Sec. 3.3.2. Another advantage of this design is a much lower cost relative to standard Roman pot designs which are at atmospheric pressure on one side, and require a pressure compensation system to combat the forces caused by the imbalance in pressure between the inside and outside of the pot. Our design also only requires a small diameter bellows and a small range of motion.

A step motor drives a cam system that moves the pot along the direc-

tion of the chimney axis. A system of bearings keeps the box movement from deviating from the direction perpendicular to the beam line. The position sensing system is based on two high precision linear potentiometers (LVDT's), one performing the primary position measurement and the second providing redundancy. The position sensor signal will be sent to the Main Control Room, where the Roman pot movement will be monitored. The whole positioning system will be capable of a displacement precision of better than 25 $\mu$m.

## 4.2 Position Detectors

Each Roman pot contains a position detector, which is used to determine the $(x, y)$ coordinate of the deflected proton at the pot position. These detectors should be very reliable as they will be located in the tunnel and consequently difficult to access. The resolution requirements are modest, since uncertainties in the beam position and location of the pot make a point resolution of better than 100 $\mu$m superfluous. The radiation environment at an $8\sigma$ distance from the beam is only about 0.03 Mrad per year of normal running, so the radiation hardness of the detector is not an overriding concern. The final detector choice should be comparable in cost to the Roman pots and should be easily integrated into the standard DØ data block and trigger.

### 4.2.1 Scintillating Fiber Detector

Figure 24 shows sketches of front and side views of the Roman pot with the position detector and trigger scintillator. The trigger scintillator consists of a $2 \times 2$ cm plastic scintillator connected to a PMT. The coincidence formed by the trigger scintillators in each spectrometer can be used in the Level 1 trigger, both for triggering and rejecting early time hits from halo. Existing scintillator and phototubes could be used for these small counters. We would likely use Level Ø phototubes from Run I which have a time resolution of 240 psec, but cannot be used in the upgraded Level Ø due to the solenoid magnetic field.

The primary detector option is a six-plane scintillating fiber detector. The detector is comprised of stacked ribbons of four fibers oriented such that the scattered proton (or anti-proton) would pass through all four fibers to maximize the light output. The stacked ribbons have a one-third ribbon width spacing. Each detector will have six views as shown in Fig. 25.

- U: with 20 ribbons oriented at 45 degrees relative to the bottom of the pot.
- U': like U but displaced from U by two-thirds of the ribbon width.
- V: built like U but rotated by 90 degrees relative to U.
- V': like V but displaced from V by two-thirds of the ribbon width.
- X: with 16 ribbons oriented perpendicular to the bottom of the pot.
- X': like X but displaced from X by two-thirds of the ribbon width.

Table 5 summarizes the position detector geometry.

| view | channels | width ($\mu$m) | gap ($\mu$m) | offset ($\mu$m) | orientation (degree) |
|---|---|---|---|---|---|
| U | 20 | 800 | 270 | - | 45 |
| U' | 20 | 800 | 270 | 540 | 45 |
| V | 20 | 800 | 270 | - | 135 |
| V' | 20 | 800 | 270 | 540 | 135 |
| X | 16 | 800 | 270 | - | 90 |
| X' | 16 | 800 | 270 | 540 | 90 |
| Total | 112 | | | | |

Table 5: Details of the detector geometry are given, where gap is the separation between channels, offset refers to the offset of the primed (') channels relative to their same view partners, and orientation is measured relative to the bottom of the pot.

The use of $0.8 \times 0.8$ mm square scintillating fibers would allow a theoretical resolution of about 80 $\mu$m. The estimated radiation dose of the detector is 0.03 Mrad per year of normal running. A full hit by the proton beam corresponds to 0.3 Mrad, or ten years of normal run. Studies have shown that a 1 Mrad dose reduces the fiber attenuation length to 40% of its original value [42]. However, due to the short length of our fibers (2 cm) the reduction in attenuation length is not important even with several beam accidents.

### 4.2.2 Fiber Readout and Trigger

The scintillating fibers are connected to clear fibers that are bundled together in groups of four and connected to one channel of the MAPMT as shown in Fig. 26. Four fibers per channel will give about 10 photoelectrons and fit comfortably within the pixel size of the MAPMT. There will be 112 channels per pot, so seven 16 channel tubes will be required for each pot (126 in all). The upper right side of Fig. 26 shows a front view of the 16 channel HAMAMATSU H6568 MAPMT. This MAPMT presents good gain uniformity among its 16 anodes with negligible cross-talk and has a pitch of 4.5 mm. The lower right part of the figure shows how the four fiber arrangement interfaces with an anode.

The MAPMT's can be read out by a standard Central Fiber Tracker (CFT) trigger board, with one trigger board required for each of the nine spectrometers. The total number of channels needed per spectrometer is 224 (112 per pot) which is well below the trigger board limit of 512 channels. A schematic of the trigger board as applied to the outputs for the $P_1$ spectrometer is shown in Fig. 27. The signal from the MAPMT will likely have to be attenuated by at least a factor of ten since the gain expected from the MAPMT is much greater than that of the VLPC, for which the boards were designed. The signals will be passed through the existing front-end chip, modulo the minor modifications to the components necessitated by the exact signal size and shape. These boards were designed to allow for different input signals since they are being used by the central and forward preshower detectors in addition to the central fiber tracker, thus the modification of these components will not be difficult or costly. The front-end chip outputs signals to the SVX-II chip for digitization. The SVX-II chip will then store the information from the fiber hits in the standard event data block. The front-end chip also outputs a TTL signal for use in the trigger logic.

The Level 1 trigger logic is formed in gate array chips which combine the hit plane information along with a table-lookup incorporating the transport matrix equations to give the $\xi$ and $|t|$ of the track. A preliminary study of the tracking equations indicates that about 500 equations will be necessary to specify a typical $\xi$ and $|t|$ range, well below the 8000 equations available on the trigger board. The total time required for the FPD Level 1 decision is about 800 nsec, 400 nsec for proton transit and return of the signal to the DØ region and another 400 nsec for the trigger logic and transit to the Level 1 framework. This is well within the 4.2 $\mu$sec time allowed for a Level 1 decision. The Level 1 framework will automatically synchronize the FPD

decision with all other Level 1 decisions, so timing will not be a problem.

The nine CFT trigger cards (one for each spectrometer) will transmit their trigger decisions to the FPD trigger manager. The manager will combine these independent trigger decisions into L1 "and/or" terms for the L1 Framework. The FPD trigger manager will be housed in a single crate. This crate will be a smaller version of the CFT and Muon L1 trigger managers and will not require additional design or engineering.

The trigger operation is best illustrated with a simple example. Consider a single diffractive interaction trigger which requires a coincidence of trigger scintillator hits along with a track in any one of the nine spectrometers. First, each spectrometer will transmit all signals (MAPMT and trigger scintillator hits) to the trigger cards. Each card has been preprogrammed to trigger if the spectrometer scintillator planes show coincident hits, and if hits in the tracking planes are consistent with a trajectory that has $\xi$ and $|t|$ values within a specified range. A trigger card then reports the occurrence of the scintillator coincidence and valid track to the trigger manager.[7] The trigger manager then polls all spectrometers to see if any one of the spectrometers has a valid trigger, and provides a logical OR of the results to the L1 Framework. Double pomeron exchange or elastic triggers would be generated by requiring pairs of spectrometers to trigger. We expect approximately ten of the 256 Level 1 "and/or" terms will be utilized by the FPD.

This readout system has the great advantage of using existing DØ trigger boards such that the data storage and triggering are completely DØ standard.

### 4.2.3 Related Detector Options and Testing

We have begun testing of prototype detectors described in the previous section. In the interests of optimizing the detector, we are also studying closely related designs. One possible minor modification to the above design is to use a small piece of plastic scintillator joined to the clear fibers for each channel, rather than making a ribbon with four scintillating fibers.

Another possibility is to use small scintillator pieces with wavelength shifting fiber (WLS) to collect the light from each channel and guide it to the MAPMT instead of using clear fiber light guides. A single channel with

[7] Given the abundance of equations available in the trigger cards, 2 $\xi$ thresholds and 2 $|t|$ thresholds should be available. In that case, each card would report four outcomes to the trigger manager.

a small grooved piece of plastic scintillator containing a WLS fiber is shown in Fig. 28. The fiber has both ends polished with one end connected to the phototube and the other end sputtered with aluminum to increase reflection and light collection.

This design is attractive since it would reduce the volume occupied by the fibers in the interior of the pot and also allow thinner fibers ($400\mu$m) that have a smaller bending radius. This would imply a reduction of the pot size and cost.

The 20 channels per detector plane (either made of a ribbon of fibers or of a small piece of plastic scintillator) will be assembled in a frame that will hold them in the correct position and give strength to the assembly. Figure 29 shows a U channel frame. The frame was made in a two stage process: first a plastic mold was made from an aluminum prototype, then the final frame was cast in polyurathane from the mold. The frame consists of a series of 850 $\mu$m wide grooves to hold the 800 $\mu$ active detector, with each groove separated by a 220 $\mu$m fin.

In conclusion, testing to optimize the design and study construction issues is underway. The detector technologies are well-known and present no technical risk.

### 4.2.4 Consideration of Other Detector Technologies

We have also considered other detector options, such as silicon or gas microstrip detectors. The silicon option is at first glance very attractive. One could use existing F-disk or H-disk detector for little additional cost with resolution clearly superior to the fibers. There are serious drawbacks, however, which make them less than optimal. The first problem is the 1 mm dead area at the bottom of the wafer, primarily due to the guard ring structure. Since the acceptance is critically dependent on the distance from the beam, this is a serious defect. Another problem is that the silicon is not fast enough to be used as a Level 1 trigger. This means that the triggering capability would have to be developed as a preprocessor for Level 2, which would result in a significant cost, or delayed until Level 3, which would cause bandwidth concerns. The silicon is also subject to radiation damage in case of accidental beam loss. The gas microstrip detector suffers from an even worse dead area of about 2 mm. It might be possible to reduce this with some research and development, but the cost would be significant, and it is unclear how the readout would fit into the standard DØ framework.

We have also examined other readout options, including the VLPC cas-

settes used by the Central Fiber Tracker. This option would require two new cryostats located in the tunnel, since the distance from the pots to the VLPC cryostat is too large compared to the attenuation length of the fiber. A prototype of a small cryostat which would be suitable for the task is being built for CFT tests. The estimated cost of the cryostats and controls coupled with the added complication of using the accelerator helium for cooling, makes this option less attractive then the MAPMT's.

In conclusion, we have not been able to identify a cheaper, more reliable option than a scintillating fiber detector readout with multi-channel phototubes.

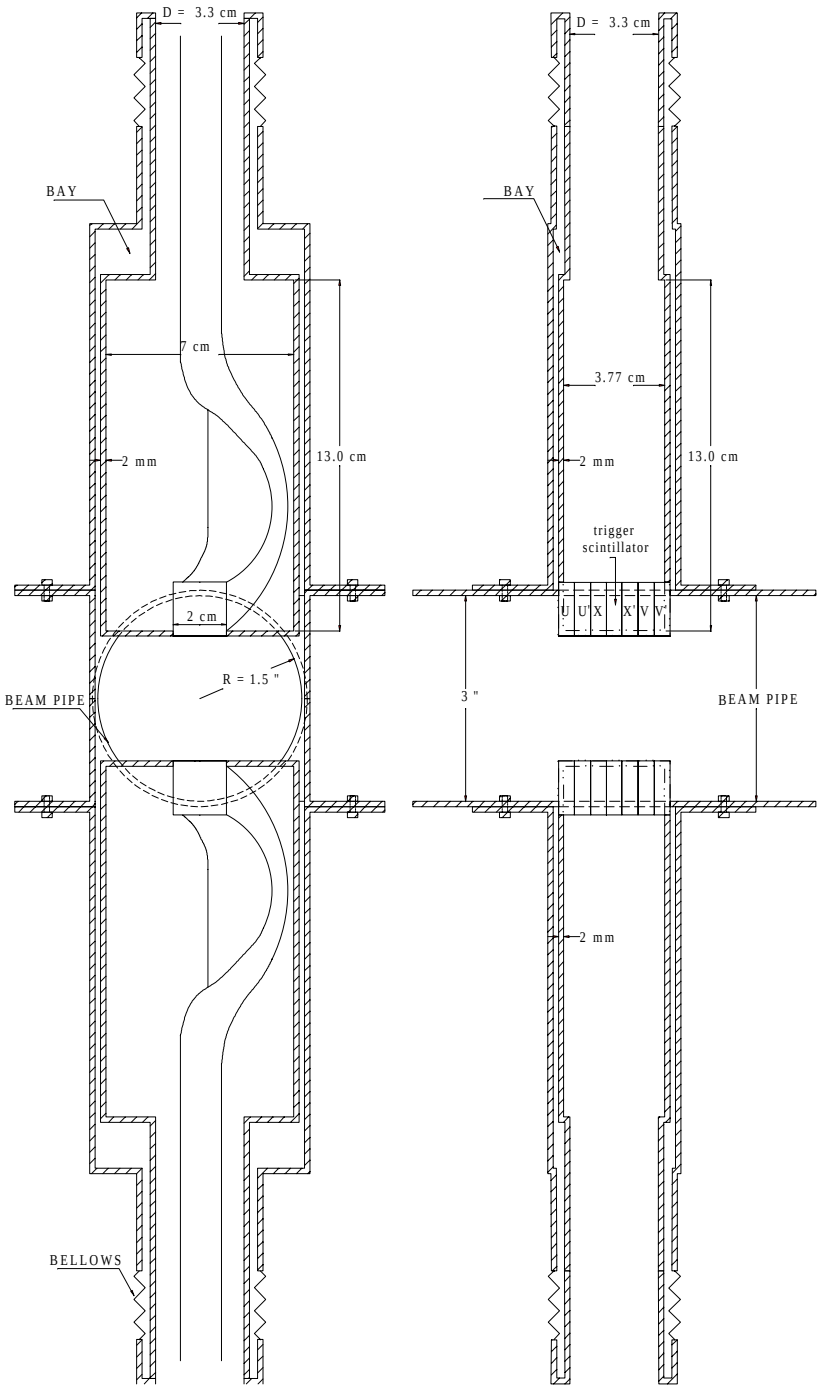


Figure 23: A front view and side view of the conceptual design for a pair of Roman pots. The pots are located in a bay area inside the beam pipe. A thin window covers the 2 cm active area of the detector. The length of the detector in the beam direction is only about 3.8 cm.

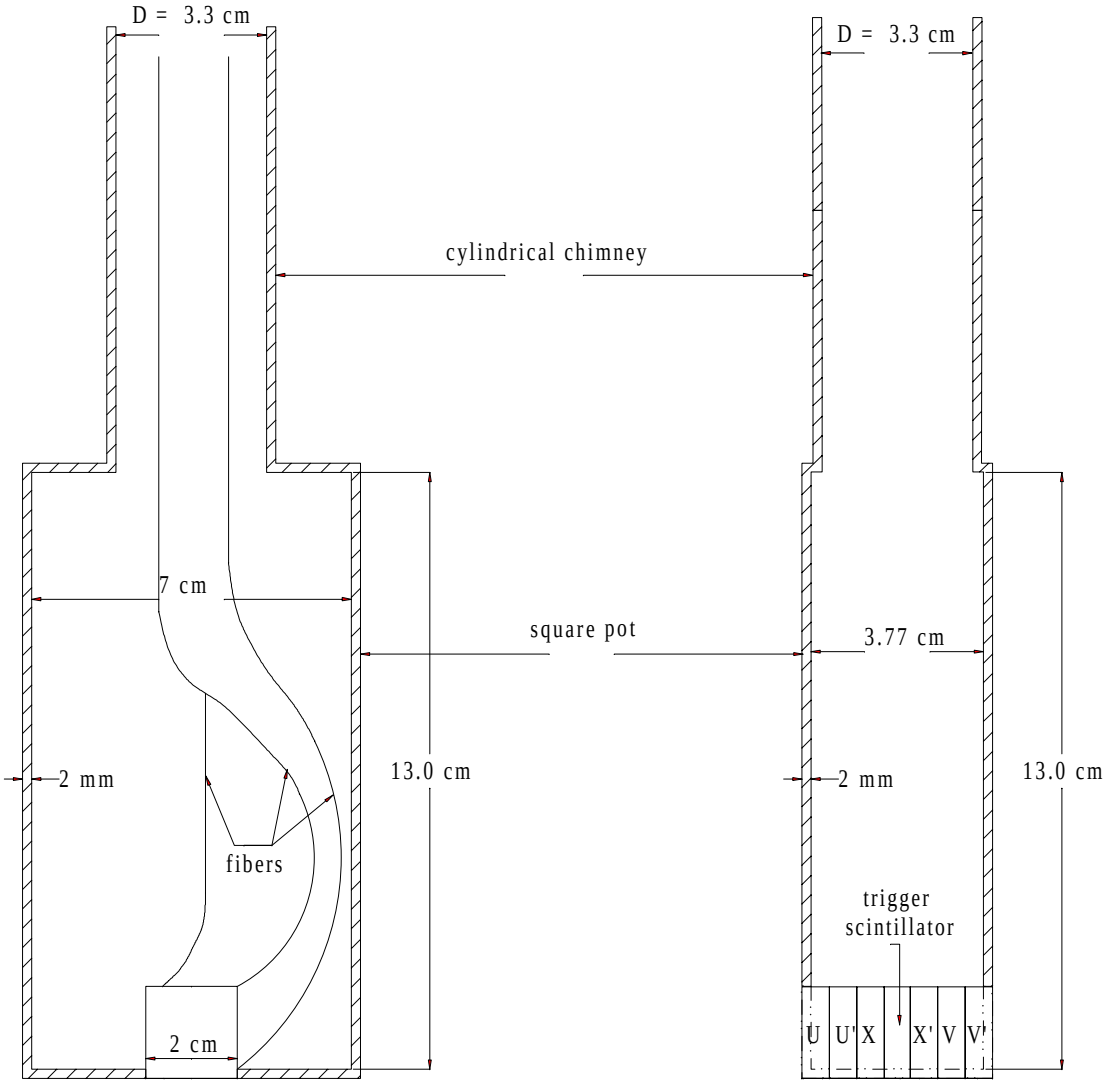


Figure 24: A front and side view of the detector described in the text.

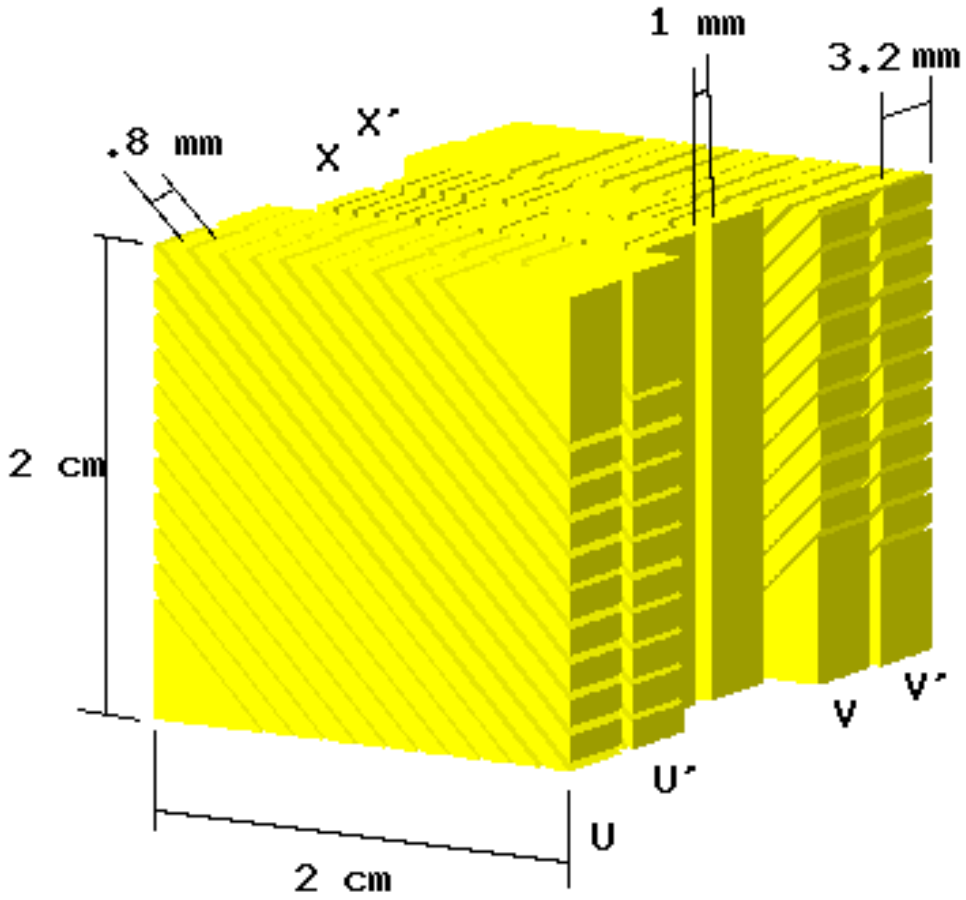


Figure 25: The six-plane scintillation detector and frames described in the text.

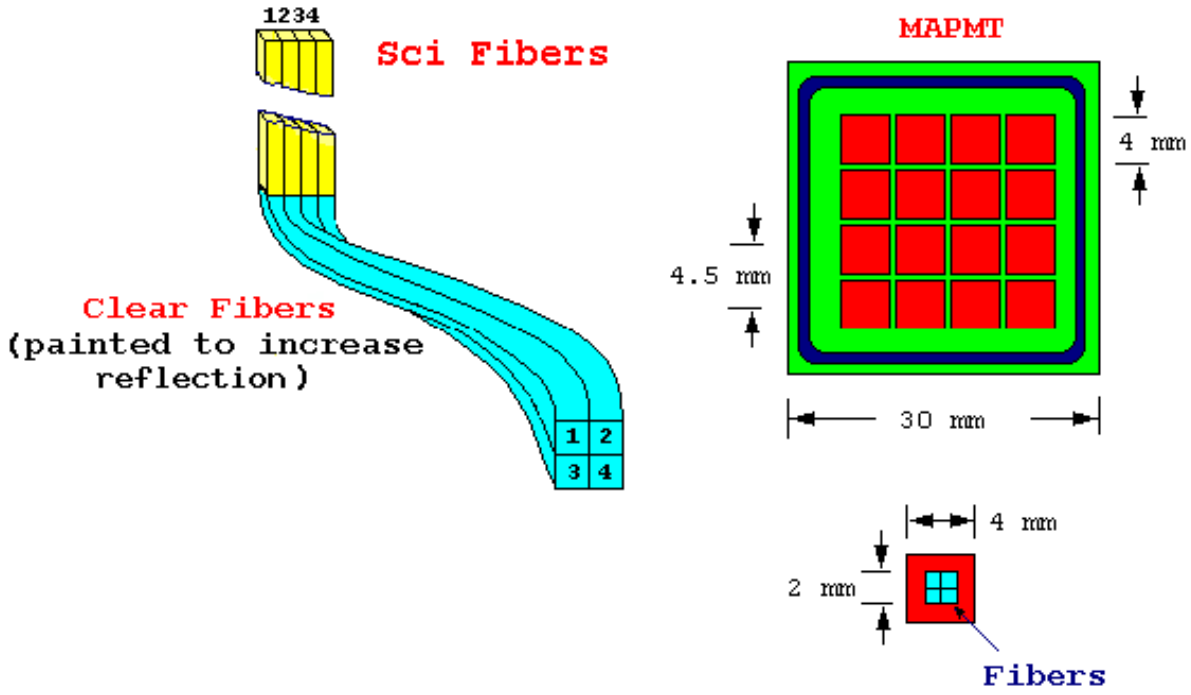


Figure 26: The interface of clear and scintillating fibers and the MAPMT.

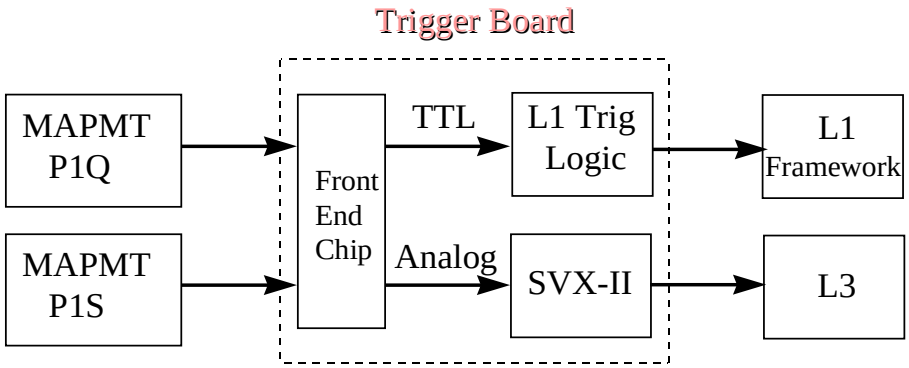


Figure 27: A schematic diagram of the readout of the scintillating fiber detectors.

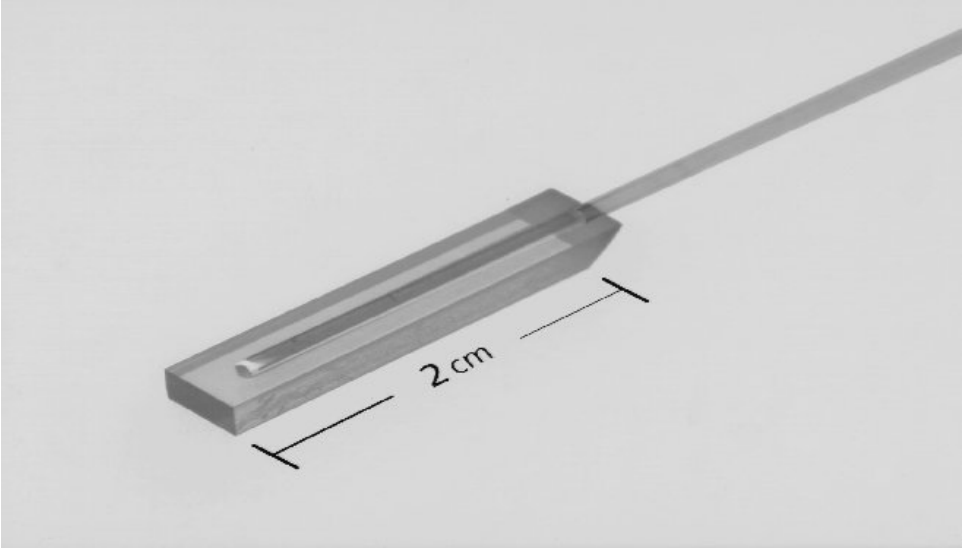


Figure 28: Picture of the detector option showing a wave length shifter (WLS) fiber attached to a piece of plastic scintillator.

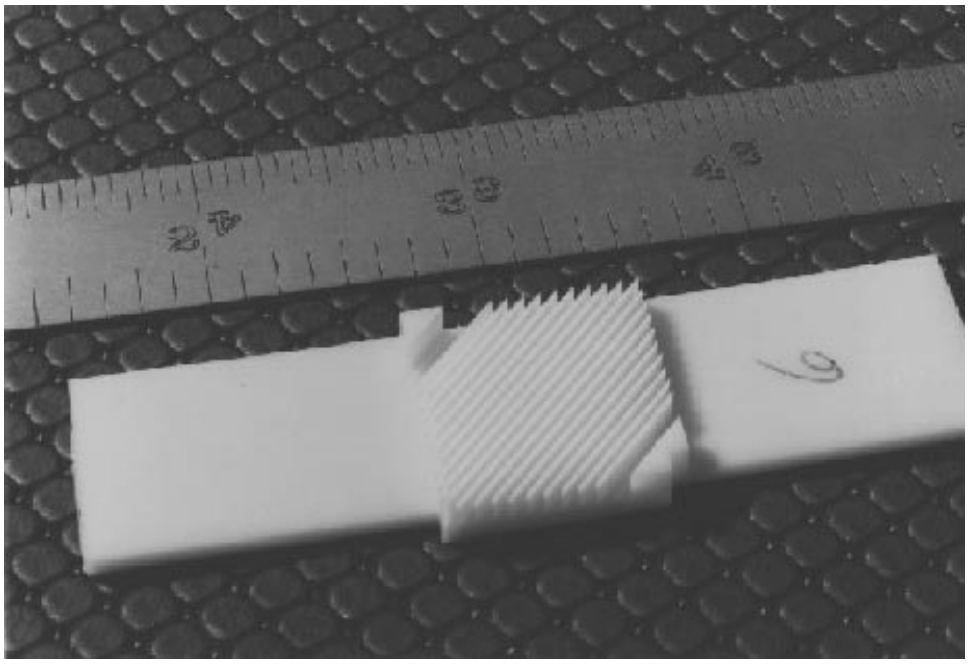

Figure 29: Picture of the plastic frame designed to align and secure the individual channels, whether they are composed of a ribbon of fibers or a small piece of plastic scintillator.

# 5 Data Taking and Analysis

## 5.1 Roman Pot Insertion Procedure

While it is clear that a procedure for inserting the pots will have to be developed based on actual experience, there are a few general guidelines that can be addressed here.

### 5.1.1 Roman Pot Location

The desired location of the pots is as close to the beam as possible while maintaining acceptable halo rates in the pots and backgrounds at DØ. Shortly after the start of each store, once scraping is completed and the beams are stable, it will be possible to insert the pots. The halo rates will be monitored by the trigger scintillator as the pots are slowly moved in (full range of motion should be about one minute). The point of closest approach will be unambiguous, signalled by a rather sharp increase in the rates. The pots can then be slightly withdrawn so that the rates will be acceptable for data taking. It will be possible to calculate how many $\sigma$ this position corresponds to using Beam Position Monitors (BPM's). The exact details of this procedure will be worked out in conjunction with the Beams Division. Similar procedures will be used for location of the collimators in Run II on a store-by-store basis.

Opposite side pots should be moved in as symmetrically as possible. A sample of elastic events can then be used off-line to determine the position of the beam, using the rates of elastic events in each pair of pots. An alternate procedure involves plotting the rates versus position as the pots are inserted, and then fitting a gaussian to the central part of the distribution to determine the beam location. We estimate a beam position uncertainty of about 100 $\mu$m, which is comparable to the position resolution of the detector and has been included in the momentum resolution calculation discussed in Sec. 3.3.4.

These procedures to determine the beam position can be applied (with minor modifications) even in a crossing angle case where the pots are not symmetrically located, but the error will be a little larger. The trigger scintillators can be used to monitor beam stability as well. These procedures can easily be automated based on experience developed during the commissioning of the upgraded DØ detector.

### 5.1.2 Accelerator Background at DØ

With no Roman pots, the accelerator-induced background is expected to be at most a few percent of the background from $p\overline{p}$ interactions. The DØ sub-detector most sensitive to accelerator related background is the forward muon spectrometer. Studies have been performed to quantify the increase in background due to the Roman pots compared to the baseline case with no pots.

A contribution to background rates of beam halo interactions with the pots is calculated assuming an intensity of $10^{13}$ protons per bunch and $10^{12}$ anti-protons per bunch and a luminosity of $1 \cdot 10^{32}$ cm$^{-2}s^{-1}$ (as in the halo studies). The halo protons scattered by the pots and secondary particles generated in inelastic nuclear interactions with the pots and accelerator components are then passed through detailed simulations with the MARS code. These simulations combine the magnetic fields and the pot, separator, quadrupole, dipole, tunnel, shielding, and DØ forward muon spectrometer geometry, yielding a three dimensional distribution of particles entering the DØ sub-detectors.[8] The ratio of the number of hits from accelerator background in the muon chambers (located at 6, 8, and 10 meters from the interaction point) with and without Roman pots is then determined. This ratio is about 4.5 for $8\sigma$ pot positions and 1.5 for $9\sigma$ pot positions, implying a total increase in background rates of at most 15% for $8\sigma$ and a few percent for $9\sigma$. The effect of a small increase in the background rates to the muon system should be minor. The pixel trigger counters for the muon system will have 1 nsec time resolution and a 20 nsec gate, and thus will be able to distinguish between hits from halo and from $p\overline{p}$ interactions.

Although previous Roman pot detectors have run with no discernible impact on nearby central detectors, and the overall effect of the increased background should be minor, one could consider adding extra shielding in the tunnel to be conservative. The background rates can be reduced by a factor of three by simply adding 2 feet of concrete or sandbag shielding to the 6 foot wall located at the tunnel-hall interface 10 meters from the interaction region. The conclusion from the background studies is consistent with that of the halo studies: the pots can likely be positioned between 8 and $9\sigma$. The actual running position will clearly have to be determined experimentally.

[8] At this time only the forward muon detector has been simulated, but a second stage which couples the MARS simulation with a GEANT simulation of the entire DØ detector is underway.

### 5.1.3 Monitoring Backgrounds at DØ

It will be important to monitor the background rates at DØ to ensure that the pots do not have a significant effect on the standard DØ physics program. This should be possible without additional instrumentation. The rates in the trigger scintillator in the pots will give a good measurement of overall halo rates. The rates in the muon pixel counters will give a measurement of accelerator losses and can be measured before and after pot insertion. The inner ring of the 10 meter pixel counters, for example, should be quite sensitive to changes in accelerator background.

The Level Ø counters located in between the central and end cryostats and covering $2.5 < |\eta| < 4.5$ can give rate information on small angle background from the pots, since this background will sometimes interact with the beam pipe and give extra Level Ø hits. The SVX detector current, which will be closely monitored in any case, can also be used to verify that the losses from the pots have a small overall effect.

We will use the standard DØ alarm system to send a warning if any of these rates deviates from a nominal range; the pots can then be retracted if necessary.

## 5.2 Data Taking Strategy

The FPD is designed to be a sub-detector of DØ and will be well-integrated into the DØ trigger framework. Due to the relatively small number of channels (about 2000 compared to hundreds of thousands for other sub-detectors), this detector will have a negligible effect on the event size. It should be read out on every event since any standard type of physics process below mass threshold can be produced diffractively.

It will also be necessary to have a few dedicated triggers which demand tracks at the trigger level. Dedicated triggers will be required for

- Diffractive jet production. The low $E_T$ jet cross section is too large to have an unprescaled diffractive jet trigger unless a track requirement is explicitly included. A diffractive jet trigger would combine a low $E_T$ cluster with a track in a $p$ or $\overline{p}$ spectrometer.

- Double pomeron exchange. This will require tracks in $p$ and $\overline{p}$ spectrometers, as well as an $E_T$ cluster for the hard double pomeron exchange case.

- Inclusive single diffraction. This prescaled trigger will be necessary to understand the operation of the FPD, as well as for soft single diffraction studies and ratios of diffractive jet to inclusive diffraction, which allows for the cancellation of many systematic uncertainties.

- Elastic scattering. This requires tracks in diagonally opposite spectrometers. A sample of elastic events should be accumulated each run for alignment purposes and luminosity monitoring. These events should be quiet in all the other detectors and could be written at a high rate without requiring much bandwidth.

To minimize the bandwidth for these dedicated triggers, the capability to cut on $\xi$ at Level 1 is essential (See Sec. 4.2.2). This allows the different triggers to only accept tracks in the kinematic range of interest. In addition to the requirement of a $p$ or $\overline{p}$ (and in some cases jets), the dedicated triggers must include elements to reject multiple interaction and halo backgrounds, which will be discussed in the following section prior to the discussion of trigger rates and data samples.

Although the bulk of data taking will be done during typical collider running conditions, it may be advantageous to take occasional low luminosity runs or special runs for systematic studies. It will be useful to map out the acceptance contours and a few dedicated runs are typically optimal for high cross section and alignment studies.

## 5.3 Multiple Interactions and Background

A serious concern about triggering on hard diffraction is the frequency of multiple $p\overline{p}$ interactions in the same bunch crossing. There are two types of multiple interactions that are of concern:

1. The superposition of a hard single diffractive event with a minimum bias event.

2. The superposition of a standard single diffractive event with a hard scattering event (pile-up background).

Unlike pile-up (discussed in Sec. 5.3.1), the occurrence of an extra minimum bias interaction in a hard diffractive event is not a background. It does, however, obscure some of the properties of the diffractive events by changing the multiplicity distribution (filling in the rapidity gap) and biasing the energy flow of the event. For high cross section processes we have the luxury

of rejecting these events online, and can obtain a good sample of single interaction events in order to properly study the diffractive final states. This can be achieved with single interaction triggers using the upgraded Level Ø detector in a similar manner as in Run I.[9] We would pass the event if there were

- No hits on one side of the Level Ø beam hodoscope scintillators. This is the typical configuration for low to intermediate mass single diffractive events.
- Level Ø hits on both sides, but with a timing consistent with a single interaction hypothesis. Higher mass diffractive events or diffractive events where the interacting parton from the pomeron carries a large fraction of the pomeron momentum will often give hits on both sides of Level Ø.

This single interaction requirement can be implemented at Level 1, so these multiple interaction events will have minimal impact on the bandwidth. The residual multiple interaction contamination in this sample should be small (about 10% from Run I studies) and can be cleaned up further at Level 3 or offline by demanding that the silicon vertex detector find only one primary vertex, which will give a residual contamination of $< 1\%$.

The probability $\mathrm{P}(n = 0)$ of no extra interaction in addition to a hard scattering is easily calculated using the following equations, which give the average number of extra interactions $\overline{n}$ in terms of the cross section $\sigma$, instantaneous luminosity $\mathcal{L}$, period $T$, and number of bunches $N_B$.

$$\overline{n} = \sigma \cdot \mathcal{L} \cdot T/N_B \tag{7}$$

$$P(n = 0) = \mathrm{e}^{-\overline{n}} \tag{8}$$

The second column in Table 6 (labelled Min Bias) shows the probability of no extra minimum bias interactions as a function of luminosity using a minimum bias cross section of $\sigma = 47$ mb, $T = 2.094 \times 10^{-5}$ s, and 36 bunches. The single interaction fraction is seen to be quite appreciable at lower luminosities, but falls quickly with luminosity. For rare processes such as diffractive $W$ production it would be undesirable to impose a single interaction requirement at the trigger level, due to the loss in statistics. It

[9] The upgraded Level Ø detector is currently being developed and we do not have sufficient information yet to do detailed simulations of its performance, but its characteristics should be similar to those of the Run I Level Ø detector.

| Lum | Min Bias $\sigma = 47$ mb | SD $\sigma = 10$ mb | SD($\xi > 0.004$) $\sigma = 2$ mb | SD($\xi > 0.01$) $\sigma = 1$ mb | |
|---|---|---|---|---|---|
| ($\mathrm{cm}^{-2}\mathrm{s}^{-1}$) | P($n = 0$) | P($n = 0$) | P($n = 0$) | P($n = 0$) | P($n \geq 2$) |
| 2E31 | 0.58 | 0.89 | 0.98 | 0.99 | 0.000067 |
| 4E31 | 0.34 | 0.79 | 0.95 | 0.98 | 0.00027 |
| 6E31 | 0.19 | 0.71 | 0.93 | 0.97 | 0.00060 |
| 8E31 | 0.11 | 0.63 | 0.91 | 0.95 | 0.0010 |

Table 6: Single interaction fraction P($n = 0$) versus instantaneous luminosity for minimum bias and single diffractive (SD) cross sections, assuming 36 bunches. The probability of two or more extra interactions P($n \geq 2$) is also given for $\sigma = 1$ mb.

is more sensible to read out the Roman pot detectors for all events and just impose single interaction requirements on the higher cross section processes. Of course, there will be an appreciable fraction of rare events with a single interaction that can be studied in more detail.

### 5.3.1 Pile-up Background

Pile-up, the background due to the superposition of a low mass diffractive event with a hard scattering event, is a more serious concern since this combination can fake a hard diffractive signal. Using the two-arm ($p$ and $\overline{p}$) single diffractive (SD) cross section of $\sigma = 10$ mb, we see that there will be an appreciable pile-up background for the quadrupole spectrometers (the fake background for the dipole spectrometer is relatively less important due to the acceptance being weighted towards higher $\xi$ where the fake background is negligible). For example, from the third column of Table 6 at 4E31 luminosity 21% of all events (1−P($n = 0$)) will have at least one extra single diffractive event. Fortunately, this background is dominated by very low mass diffraction which could not produce jets and can easily be rejected at Level 1 by a cut such as $\xi > 0.004$, which will reduce the effective cross section to about 2 mb [21]. Applying this cut reduces the overlap of diffractive events with dijet events to a few percent (5% at 4E31). The aforementioned single interaction requirement will reduce this background by about a factor of 10 based on Run I experience. Note that virtually all single diffractive events with $\xi > 0.004$ ($M_X > 126$ GeV/$c^2$) will give enough hits in the Level Ø counters for this requirement to be effective. With these simple cuts the fake background is reduced to about 0.5% of dijet events, which is

on the order of the expected 0.3–1% hard diffractive dijet signal [11]. As shown in Sec. 5.4, the Level 1 rates implied by this level of background are acceptable after the proton acceptance is taken into account. At Level 3 this background can be reduced to near zero as discussed below.

The hard double pomeron background, due to the pile-up of two opposite side single diffractive events with a dijet event, is also manageable. A tighter cut requiring that $\xi > 0.01$ would likely be used for double pomeron events. Since only about $M_X = \sqrt{\xi_1 \cdot \xi_2}\sqrt{s}$ is available for jet production (for $\xi_1 = \xi_2 = 0.01$ this gives an $M_X = 20$ GeV/$c^2$), there will be no contribution to jet cross sections from lower $\xi$ values, but a large contribution to the pile-up background. The column in Table 6 labelled P($n \geq 2$) shows the probability of having two or more single diffractive events for a diffractive cross section of 1 mb is 0.00027. This gives a background more than an order of magnitude greater than the expected signal for hard double pomeron exchange, which is likely to be a few millionths of the dijet cross section [11]. Although this absolute rate is already small and additional cuts are not strictly necessary, we would still apply a single interaction requirement to reduce the contamination at Level 1 to the same order as the signal. The same arguments apply to background from two soft single diffractive events plus a dijet event or one hard single diffractive dijet event and one soft jet single diffractive event.

At Level 3 (or offline in the case of diffractive $W$ bosons) there will be other tools available for identifying pile-up background which will be combined into a single interaction algorithm or tool:

- The new silicon tracking detector should be very efficient at finding multiple vertices ($> 99\%$) and can thus reject multiple interaction events for those interactions that have tracks with $\eta < 2.5$. The $\xi$ cuts suggested above will already ensure that the events will typically have several central tracks.

- The event interaction time from the trigger scintillators can be compared to the interaction time from Level Ø to determine whether the times are consistent with coming from the same interaction. With a single tube resolution of 240 ps, we expect a 170 ps time resolution for the two trigger counters. The Level Ø counters typically will have several counters hit and are expected to give a resolution of 100 ps. Convoluting these distributions with the time distribution of the event (about 1 nsec) and demanding a two sigma separation gives a rejection factor of three. This cut would be particularly useful for rejecting

diffractive events where the diffractive system is produced at small angles $\eta > 2.5$ for which the multiple vertex cut is ineffective.

- Conservation of longitudinal momentum can be imposed by requiring that the sum of the momentum of the trigger proton and the longitudinal energy in the DØ calorimeter on the trigger side is less than the initial 1 TeV beam momentum (within resolution). This is a very effective cut, particularly for low $\xi$ (for example with $\xi = 0.01$ the proton alone contributes 990 GeV/$c$ to the longitudinal momentum). Essentially, this makes use of the fact that a pile-up event will have a beam remnant and a diffractive event will have none to reject pile-up events. An equivalent cut for the UA8 collaboration was very successful and the FPD momentum resolution and DØ energy resolution are greatly superior.

A loose rapidity gap requirement could also be implemented. As an example consider the multiplicity distribution in Fig. 3. A cut of $n_{EM} < 3$ would provide a rejection factor of 100 on fake background events while preserving all rapidity gap events. We would be reluctant to adopt a rapidity gap cut online in the hard diffractive triggers except in the unlikely event that it proves absolutely necessary to control the rates, since there would potentially be some biases to the physics. For inclusive double pomeron exchange, rapidity gap requirements likely will be used due to higher backgrounds and less concern about biases.

Although lower luminosity is optimal for dedicated hard diffractive triggers, there is still an appreciable single interaction cross section at very high luminosity and there are many handles for rejecting pile-up background.

### 5.3.2 Halo Background

A preliminary study of the correlation of halo hits was performed to determine the background from halo. This study used the Run II lattice and quadrupole pots with a displacement of $8\sigma$. Since we will have accurate timing from the trigger scintillators, we can reject in-time halo particles which leave early time hits in the diagonally opposite quadrupole spectrometer. Halo background is very sharply peaked at $\xi = 0$ as shown below, and is thus not a concern for the dipole spectrometer. About 25% of the tracks gave hits in both pots in a spectrometer (correlated hits), while 75% gave hits in only one pot (uncorrelated hits). To calculate the acceptance for halo hits faking a track which we cannot reject from timing, we use the following

equation

$$A_H = 0.25H \cdot A_C + (0.75H \cdot A_U)^2 \quad (9)$$

where $A_H$ is the total halo acceptance, $A_C$ is the acceptance for correlated halo, $A_U$ is the acceptance for uncorrelated halo, and H is the fraction of events with at least one halo hit.

We pessimistically assume that a halo hit or track must pass through both opposite side pots to be rejected. For the correlated tracks, $A_C = 0.02$ since $> 98\%$ of tracks had early time hits in both pots of the diagonally opposite spectrometer. For the uncorrelated hits (which pass through only one pot in-time), $A_U = 0.5$, but uncorrelated hits can only fake a track if there is one accepted hit in each pot for the same event. Assuming a 100 kHZ halo rate with a 1.7 MHz crossing rate, we find that about 6% of all interactions have a halo hit ($H = 0.06$). Substituting these values gives $A_H = 0.0008$, which means that for pessimistic assumptions about 0.0008 of all interactions will have an accepted halo track. Halo can only fake diffractive jet events when superimposed with a dijet event, so only 0.08% of dijet events will have a halo track. As shown in Fig. 30 the halo tracks are sharply peaked near the beam momentum of 1000 GeV/$c$ ($\xi = 0$) and will largely be removed by the demand of a track with $\xi > 0.004$. The uncorrelated hits will also be effectively rejected by demanding a valid track, since they dominantly form unphysical combinations. With a resolution $\delta\xi = 0.0012$ the chance of $\xi = 0$ fluctuating to $> 0.004$ is less than 0.1%, but we assume only a factor of 50 rejection. The L1 halo rate of $1.6 \cdot 10^{-5}$ of the dijet cross section will thus be smaller than the signal rate, which is about $3 \cdot 10^{-5}$ of the dijet cross section (assuming a track acceptance of 1% and a signal of 0.3%).

Although the silicon vertex information will not be useful for rejecting halo, the other components of the L3 single interaction tool will be. The rejection factor from scintillator timing which was three in the multiple interaction case will be at least four due to the broader $z$ distribution from halo interactions. The longitudinal momentum cut will clearly be very effective as a proton with $\xi = 0.004$ carries 996 GeV/$c$. We estimate greater than a factor of 10 rejection from this cut. Halo background will clearly not be a problem for hard diffractive processes.

## 5.4 Triggering and Event Samples

The FPD will be used to study the physics topics discussed in Section 2. Examples of the trigger terms for the primary physics topics that require

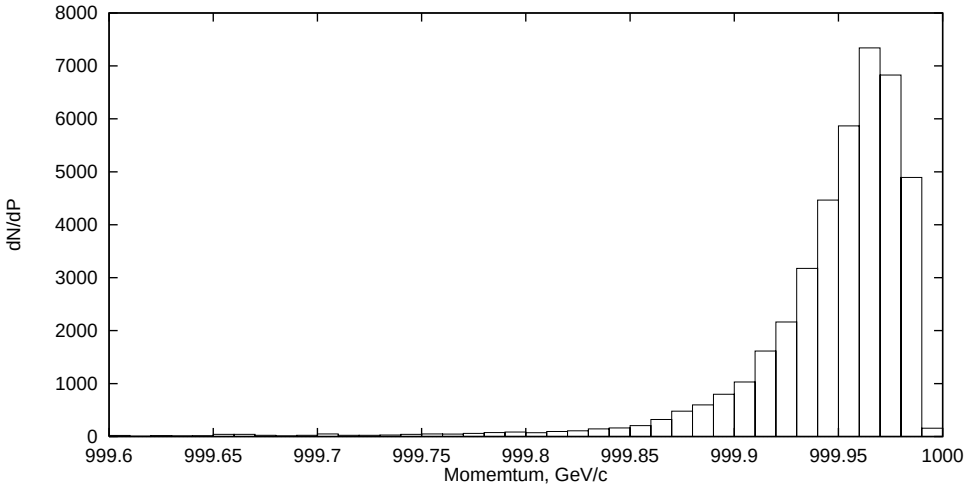


Figure 30: The momentum distribution of halo particles that hit the Roman pots.

dedicated triggers are given in Table 7. These terms are described in detail below:

- "Track" refers to a track required with a certain momentum fraction. For the hard diffraction trigger the track can be in any spectrometer, for the double pomeron triggers both $p$ and $\overline{p}$ tracks are required.
- "Halo Veto" refers to the veto on early hits in the diagonal opposite spectrometer
- "LØ Single Interaction" is the requirement that the Level Ø counters yield a timing consistent with a single event hypothesis.
- "Tower" refers to a trigger tower which is $0.2 \times 0.2$ in $\eta \times \phi$.
- "LØ Veto" demands that there are no hits in either side of LØ (rapidity gap requirement).
- "Single Interaction Tool" is a Level 3 routine that uses the full detector information to reject multiple interactions as discussed in the previous

| Trigger | L1 Terms | L3 Terms |
|---|---|---|
| Hard Diffraction | Track($0.97 < x < 0.996$)·Two 2 GeV Towers · Halo Veto·LØ Single Interaction | 1 Jet $E_T > 15$ GeV· Single Interaction Tool |
| Hard Double Pomeron | Track($p$,$\overline{p}$,$0.95 < x < 0.99$)·Two 2 GeV Towers · Halo Veto·LØ Single Interaction | 1 Jet $E_T > 10$ GeV· Single Interaction Tool |
| Double Pomeron | Tk($p$,$\overline{p}$,$0.97 < x < 0.996$)·Halo Veto·LØ Veto | X·SI Tool |

Table 7: Details of primary dedicated triggers.

| | Trigger Rates (Hz) | | | | |
|---|---|---|---|---|---|
| Trigger | L1 Physics | L1 Bkgd | L3 Physics | L3 Bkgd | Events/fb$^{-1}$ |
| Hard SD | 4.0 | 2.2 | 0.08 | 0.0005 | 500,000 |
| Hard DP | 0.002 | 0.001 | 0.0004 | 0.000002 | 2,500 |
| Inclusive DP | 0.07 | 0.07 | 0.001 | $\approx 0$ | 6,000 |

Table 8: Trigger rates (Hz), backgrounds, and number of events for hard single diffraction, hard double pomeron, and inclusive double pomeron exchange.

section.

- "X" refers to some level of activity in the detector, such as a central fiber track, some number of hits in the silicon vertex detector, etc.

In addition to these triggers, prescaled elastic and single diffractive triggers will be taken to monitor the FPD performance.

### 5.4.1 Trigger Rates

The trigger rates for hard diffraction, hard double pomeron exchange, and inclusive double pomeron exchange are discussed in this section. Each topic has a detailed estimate of the physics and background rates showing the effect of each trigger term. There is a table summarizing each topic. A global summary of the rates and expected number of events is given in Table 8 for a typical 4E31 luminosity.

The Level 1 rates in Hz are given by the following expression:

$$\mathrm{L1} = \sigma \cdot \mathrm{A} \cdot \mathrm{SI} \cdot \mathcal{L} \tag{10}$$

where $\sigma$ is the L1 cross section, A is the spectrometer acceptance, SI is the single interaction acceptance factor (which ranges from 1 at low luminosity to 0.1 at high luminosity), and $\mathcal{L}$ is the luminosity in units of $10^{30}$ cm$^{-2}s^{-1}$.

- Hard Diffraction. The summary of this section is given by Table 9. The details are discussed below. The cross section for two trigger towers with $E_T > 2$ GeV was measured in Run I to be about 1000 $\mu$b. Assuming 0.3% of these events are diffractive gives a cross section of 3 $\mu$b. A cut of $\xi < 0.03$ is imposed to ensure that the data sample is dominated by pomeron exchange (some data would be taken with a relaxed cut in order to understand the non-diffractive background). The acceptance is about 1% for the quadrupole spectrometers and 20% for the dipole spectrometer over this range. Since only $\overline{p}$'s are accepted by the dipole spectrometer, the average acceptance is about 10%. A luminosity of $4 \cdot 10^{31}$ cm$^{-2}s^{-1}$ gives SI = 0.34 (from Table 6), which combined with A = 10%, yields $\mathrm{L1_{HSD}} = 4.0$ Hz.

  The multiple interaction fake rate can also be evaluated using Eq. 10, with different values of $\sigma$ and A. In this case $\sigma = 5$ $\mu$b (0.5% of the dijet cross section including the Level Ø cut as discussed in the previous section). The acceptance for quadrupole spectrometers is the same for signal and fake background, but the dipole acceptance for fake background is much lower due to the increased acceptance for higher $\xi$ which has lower background. An overall acceptance A = 3% is assumed, giving $\mathrm{L1_{MI}} = 2.0$ Hz. The same SI factor still applies, since it refers to the overlap of an extra minimum bias event, which would cause the rejection of fake background that would have otherwise passed the single interaction cut.

  For halo, $\sigma \cdot \mathrm{A} = 0.000016 \cdot 1000$ $\mu$b as discussed earlier (the 0.000016 already includes the acceptance for halo tracks), so $\mathrm{L1_{HALO}} = 0.2$ Hz.

  Unlike most DØ triggers there will be little luminosity dependence of the rates, since the rate increase from the increased luminosity is roughly cancelled by the SI acceptance factor which decreases with increasing luminosity.

  From Run I the $E_T > 15$ GeV jet cut gave a reduction of about 50, giving a Level 3 physics cross section of 2 nb, corresponding to a rate of 0.08 Hz. From the single interaction tool, we expect a rejection of greater than 100 for fake background and greater than 40 for halo background (in addition to the jet rejection which applies equally to all these samples), giving a final background rate of less than 0.0005 Hz (about 20% coming from halo).

- Hard Double Pomeron. We now apply Eq. 10 to the hard double

| | $\sigma(\mu\text{b})$ | Rate(Hz)@$4\times10^{31}$ |
|---|---|---|
| Hard Diffraction | | |
| $\sigma_{L1}(p\overline{p} \rightarrow jj)$ | 1000 | 40000 |
| $\sigma_{L1}(\text{SD}\rightarrow p+jj)$ | 3 | 120 |
| $\sigma_{L1}(\text{SD}\rightarrow p+jj)\cdot\text{A}$ | 0.3 | 12 |
| $\sigma_{L1}(\text{SD}\rightarrow p+jj)\cdot\text{A}\cdot\text{SI}$ | 0.1 | 4.0 |
| $\sigma_{L3}(\text{SD}\rightarrow p+jj)\cdot E_T > 15$ | 0.002 | 0.08 |
| MI Fake | | |
| $\sigma_{L1}(p\overline{p} \rightarrow jj)$ | 1000 | 40000 |
| $\sigma_{L1}(\text{MI}\rightarrow p+jj)$ | 50 | 2000 |
| $\sigma_{L1}(\text{MI}\rightarrow p+jj)\cdot\text{L}\emptyset$ | 5 | 200 |
| $\sigma_{L1}(\text{MI}\rightarrow p+jj)\cdot\text{L}\emptyset\cdot\text{A}$ | 0.15 | 6 |
| $\sigma_{L1}(\text{MI}\rightarrow p+jj)\cdot\text{L}\emptyset\cdot\text{A}\cdot\text{SI}$ | 0.05 | 2.0 |
| $\sigma_{L3}(\text{MI}\rightarrow p+jj)\cdot E_T > 15$ | 0.001 | 0.04 |
| $\sigma_{L3}(\text{MI}\rightarrow p+jj)\cdot E_T > 15\cdot$ L3 SI Tool($\approx$100) | 0.00001 | 0.0004 |
| Halo Fake | | |
| $\sigma_{L1}(p\overline{p} \rightarrow jj)$ | 1000 | 40000 |
| $\sigma_{L1}(\text{Halo}\rightarrow p+jj)\cdot\text{A}$ | 0.016 | 0.6 |
| $\sigma_{L1}(\text{Halo}\rightarrow p+jj)\cdot\text{A}\cdot\text{SI}$ | 0.005 | 0.2 |
| $\sigma_{L3}(\text{Halo}\rightarrow p+jj)\cdot E_T > 15$ | 0.0001 | 0.004 |
| $\sigma_{L3}(\text{Halo}\rightarrow p+jj)\cdot E_T > 15\cdot$ L3 SI Tool($\approx$40) | 0.000002 | 0.0001 |

Table 9: Cross sections and trigger rates for hard single diffraction (SD$\rightarrow$ $p+jj$) and fake backgrounds to hard single diffraction from multiple interactions (MI) and halo. The expression $p+jj$ also include the charge conjugate $\overline{p}+jj$.

pomeron case. This section is summarized by Table 10. A reasonable guess for the hard double pomeron cross section is about 1% of the hard diffractive cross section, or 0.03 $\mu$b. The acceptance is now the product of the $p$ and $\overline{p}$ acceptance. The $\overline{p}$ acceptance averaged over the range $0.01 < \xi < 0.05$ is about 50%. Combining this with the 1% $p$ acceptance yields a total acceptance of about 0.5%. Applying the luminosity and SI factor gives a L1 physics rate of 0.002 Hz.

The background to hard double pomeron exchange is dominated by the overlap of two inclusive diffractive interactions and a dijet event. At 4E31, the probability of two single diffractive events with $\xi > 0.01$ is $3 \cdot 10^{-4}$, and one-half of these cases give a $p$ and a $\overline{p}$. Assuming that 10% of these events survive the Level 1 single interaction cut gives $1.5 \cdot 10^{-5}$ of the dijet cross section or 0.015 $\mu$b. Applying the same acceptance and SI factors as for the signal gives 0.001 Hz. Other fake combinations such as a diffractive interaction with a hard single diffractive one are at least a factor of five smaller. Fake background involving halo requires either two independent halo tracks superimposed with a dijet event, or one halo track combined with a diffractive interaction and a dijet event. In either case the small acceptance combined with $\xi > 0.01$ renders this background negligible.

At Level 3, the rejection is only expected to be about a factor of 5 due to the lower $E_T$ threshold. Multiple interaction background rates should be an additional factor of 100 smaller and can safely be ignored. The total Level 3 physics cross section is thus about 10 pb.

- Inclusive Double Pomeron. This section is summarized by Table 11. The estimate for the inclusive double pomeron cross section is in the range of 10–100 $\mu$b [43]. Assume a cross section of 5 $\mu$b after applying the $\xi > 0.004$ cut. Applying a total acceptance of 0.1%, luminosity, and SI factors gives a rate of 0.07 Hz.

  The multiple interaction background requires two single diffractive events on opposite sides, which has a cross section of 50 $\mu$b (2.5% of the 2 mb cross section has a second diffractive event on the opposite side). Applying the LØ acceptance, luminosity, and SI factors give a small L1 rate of 0.07 Hz, which will be completely obliterated by the rapidity gap cut on both sides (rejection of 10,000). Fake background involving halo is negligible as in the hard double pomeron case.

  The addition of a cut on "X" (some physics activity such as tracks,

| | $\sigma(\mu\text{b})$ | Rate(Hz)@$4\times10^{31}$ |
|---|---|---|
| Hard Double Pomeron | | |
| $\sigma_{L1}(\text{DP}\rightarrow p\overline{p}+jj)$ | 0.03 | 1.2 |
| $\sigma_{L1}(\text{DP}\rightarrow p\overline{p}+jj)\cdot\text{A}$ | 0.00015 | 0.006 |
| $\sigma_{L1}(\text{DP}\rightarrow p\overline{p}+jj)\cdot\text{A}\cdot\text{SI}$ | 0.00005 | 0.002 |
| $\sigma_{L3}(\text{DP}\rightarrow p\overline{p}+jj)\cdot E_T>10$ | 0.00001 | 0.0004 |
| MI Fake | | |
| $\sigma_{L1}(\text{MI}\rightarrow p\overline{p}+jj)$ | 0.15 | 6.0 |
| $\sigma_{L1}(\text{MI}\rightarrow p\overline{p}+jj)\cdot\text{L}\emptyset$ | 0.015 | 0.6 |
| $\sigma_{L1}(\text{MI}\rightarrow p\overline{p}+jj)\cdot\text{L}\emptyset\cdot\text{A}\cdot\text{SI}$ | 0.000025 | 0.001 |
| $\sigma_{L3}(\text{MI}\rightarrow p\overline{p}+jj)\cdot E_T>10$ | 0.000005 | 0.0002 |
| $\sigma_{L3}(\text{MI}\rightarrow p\overline{p}+jj)\cdot E_T>10\cdot$ L3 SI Tool($\approx$100) | $\approx 0$ | 0.000002 |
| Halo Fake | | |
| $\sigma_{L1}(\text{Halo}\rightarrow p\overline{p}+jj)\cdot\text{A}$ | $\approx 0$ | $\approx 0$ |
| $\sigma_{L3}(\text{Halo}\rightarrow p\overline{p}+jj)$ | $\approx 0$ | $\approx 0$ |

Table 10: Cross sections and trigger rates for hard double pomeron exchange (DP$\rightarrow p\overline{p}+jj$) and fake backgrounds from multiple interactions (MI) and halo.

| | $\sigma(\mu b)$ | Rate(Hz)@$4\times10^{31}$ |
|---|---|---|
| Inclusive Double Pomeron | | |
| $\sigma_{L1}(\mathrm{DP}\rightarrow p\overline{p}+X)$ | 5.0 | 200 |
| $\sigma_{L1}(\mathrm{DP}\rightarrow p\overline{p}+X)\cdot$A | 0.005 | 0.2 |
| $\sigma_{L1}(\mathrm{DP}\rightarrow p\overline{p}+X)\cdot$A$\cdot$SI | 0.0017 | 0.07 |
| $\sigma_{L3}(\mathrm{DP}\rightarrow p\overline{p}+X)\cdot$ | | |
| Physics | 0.000025 | 0.001 |
| MI Fake | | |
| $\sigma_{L1}(\mathrm{MI}\rightarrow p\overline{p}+X)$ | 50 | 2000 |
| $\sigma_{L1}(\mathrm{MI}\rightarrow p\overline{p}+X)\cdot$L$\emptyset$ | 5 | 200 |
| $\sigma_{L1}(\mathrm{MI}\rightarrow p\overline{p}+X)\cdot$L$\emptyset\cdot$ A $\cdot$SI | 0.0017 | 0.07 |
| $\sigma_{L3}(\mathrm{MI}\rightarrow p\overline{p}+X)\cdot$ | | |
| Rap. Gap($\approx$10,000) | $\approx 0$ | $\approx 0$ |
| Halo Fake | | |
| $\sigma_{L1}(\mathrm{Halo}\rightarrow p\overline{p}+X)\cdot$A | $\approx 0$ | $\approx 0$ |
| $\sigma_{L3}(\mathrm{Halo}\rightarrow p\overline{p}+X)$ | $\approx 0$ | $\approx 0$ |

Table 11: Cross sections and trigger rates for inclusive double pomeron ($\mathrm{DP}\rightarrow p\overline{p}+X$) and fake backgrounds.

energy, or muons), since we will want to measure something in the event, will lower the physics L3 rate to an insignificant level, perhaps 0.001 Hz.

The background (Bkgd) rates are dominated by multiple interactions (see Sec. 5.3) and are seen to be small compared to the signal. While there are large uncertainties in these numbers due to the limited data on these subjects, we clearly expect to obtain large samples to carry out these analyses.

### 5.4.2 Data Samples

The Level 3 cross sections can be converted into numbers of events assuming an integrated luminosity and efficiencies. We arbitrarily assume a 50% efficiency and that 50% of the data survives offline cuts.

- Hard Diffraction. This give us a diffractive dijet data sample of 500,000 events per fb$^{-1}$ of delivered luminosity, assuming an average luminosity of 4E31 (an average luminosity of 6E31 would reduce this number

by about 40%). The world's database of tagged diffractive dijet events with $\xi < 0.05$ is measured in the hundreds and only for low $E_T$ jets. With this huge data sample we will easily be able to make cross section measurements in many $\xi$ and $|t|$ bins and have the first precision measurements of the pomeron structure from hard diffraction. If some of the assumptions are pessimistic and the accepted cross section is too high, we can always have a prescaled lower $E_T$ trigger and an unprescaled higher $E_T$ trigger. Also note that the physics rate will still include some background from non-pomeron exchanges (such as the $f_2$ meson). One of the goals of the FPD will be to attempt to understand this issue better. From Ref. [21], the inclusive non-diffractive background is estimated to be $<<$ 1% for very low $\xi$, about 15% for $\xi = 0.02$ and $> 50\%$ for $\xi = 0.05$. The non-diffractive backgrounds to hard diffraction are likely to be lower than this if the $f_2$ does not produce jets as copiously as the pomeron does [44].

- Hard Double Pomeron Exchange. The estimated sample size of 2,500 events per fb$^{-1}$ will be more than adequate for unambiguous observation of this class of events, and should allow a detailed study in a few $\xi$ and $|t|$ bins. It is clear that the number of events, not rates or backgrounds is the major concern for this physics topic. Efficiencies can be improved by relaxing the Level 1 cut somewhat. It will also be possible to combine a track in the $\overline{p}$ spectrometer with a rapidity gap on the proton side to increase the statistics by a factor of a hundred for some hard double pomeron studies. About 1% of these events would be "gold-plated" with tracks in the $p$ spectrometer as well, and could be used to study the detailed behavior of this process.

- Double Pomeron Exchange. We should obtain several thousand inclusive double pomeron events. This topology has not been studied since the ISR, and will allow "new physics" searches as discussed earlier.

- Massive States. Using efficiency estimates from Run I, we expect roughly 600,000 $W$ boson events per fb$^{-1}$, perhaps 1% of which are diffractively produced. Of these 6,000 events, about 1,500 would have tagged $\overline{p}$'s (50% of the $\overline{p}$ events) and 30 would have tagged protons. A couple hundred of these would be single interaction events. The $Z$ boson statistics are expected to be about 10 times smaller. We should also obtain 10's of thousands of tagged diffractive $b$ and $c$ events. As discussed earlier, these processes will not require special triggers or

additional bandwidth as they will simply involve reading out the FPD for all events.

These unique large data samples will allow DØ to revolutionize the field of hard diffraction.

### 5.5 Measurements Using the FPD

The large data samples obtained will be analyzed using information from the FPD in conjunction with information from other DØ sub-detectors as discussed below.

- Observation of different diffractive final states. Many of the processes which we will study have never been observed. We will be able to observe the processes that have sufficiently large cross sections and otherwise set cross section limits. For a hard diffractive process that does not require a single interaction, the cross section sensitivity will be about 0.1 pb, assuming 2 $\text{fb}^{-1}$ of exposure with a 25% efficiency, 25% acceptance (averaged over $p$'s and $\overline{p}$'s), and 10 events needed for discovery. With a single interaction requirement the minimum observable cross section will be about 0.5 pb. For the double pomeron case, the relevant acceptance is about 0.5% resulting in a 50 times higher minimum cross section of about 25 pb. For those processes that we observe, we will measure various kinematic properties such as $\xi$ and $|t|$ using the pots, and jet $E_T$ and $\eta$, energy flow, etc., using the rest of the DØ detector.

- Pomeron Structure. To study pomeron structure, the shapes of various kinematic distributions are sufficient. An example is the $\eta$ distributions of jets (shown earlier) or electrons from $W$ boson decay, both of which are sensitive to the hardness of the partons in the pomeron. Another variable, used by the UA8 Collaboration with only 100 di-jet events, is the longitudinal momentum of the two-jet system in the diffractive center of mass [5]. This variable directly reflects the imbalance between the parton in the pomeron and the parton in the proton, and, in combination with known proton PDF's, allows us to measure the pomeron structure function. We will also be able to input HERA pomeron structure functions obtained from deep-inelastic scattering and test whether they describe our data.

- Cross Sections. We can measure the cross sections of these processes in $\xi$ and $|t|$ bins. One way to express the results is to take ratios of hard diffraction and inclusive diffraction, giving quantities such as the fraction of diffractive events in a given $\xi$ and $|t|$ bin that have jets, $W$ bosons, top, etc. Each ratio can be directly compared to predictions for different pomeron structures and different quark and gluon fractions. Current Monte Carlo's assume no $|t|$ dependence of the results. We will be able to test the validity of this assumption simply by determining this ratio for a few $|t|$ bins (for a given process and $\xi$ range). This approach removes acceptance errors including the error from extrapolating to $|t| = 0$.

  We will also be able to make absolute cross section measurements. This requires accurate knowledge of our acceptance, and is where the full power of the FPD is demonstrated. By using symmetric pots (up–down or left–right), we can determine the beam position at each quadrupole station (Sec. 5.1) to an accuracy of about 100 $\mu$m. Averaging the cross sections measured in symmetric spectrometers reduces the cross section error from the beam position to a second order correction (which contributes less than 5% to the total acceptance uncertainty). We can then use well-measured tracks in the quadrupole spectrometers to calibrate the dipole spectrometer (for tracks with $|t| > 0.5$ GeV$^2$ we have a large overlap between anti-protons in the two types of spectrometers). Conversely, we can use the $|t|$ distribution measured in the dipole spectrometer (which has full $|t|$ acceptance for $\xi > 0.02$) to extrapolate the quadrupole measurements to $|t| = 0$. The dominant error in the acceptance is due to the dispersion of the beam, which causes about a 15% uncertainty integrating over the $|t|$ range of the quadrupole spectrometers. We can reduce this error significantly by measuring the dispersion using elastics and then unsmearing the $|t|$ distribution. We expect final errors on the cross section due to acceptance of a few percent in the dipole spectrometer and less than 10% in the quadrupole spectrometers.

  For a fixed $|t|$ bin, the error in the diffractive mass is $\delta\xi/2\xi$ (6% for $\xi = 0.01$, 3% for $\xi = 0.02$, etc.). Therefore, from the FPD point of view we will be able to make accurate cross section measurements. For jet cross sections we will be limited by energy scale errors which will likely be 30–50% for our $E_T$ range. Using ratios will allow us to reduce these errors. This time we will measure the fraction of jet events

above an $E_T$ threshold that are diffractive (similar to the rapidity gap measurements), making us insensitive to energy scale errors. We thus expect to measure all cross sections (or ratios of cross sections) with errors of 10% or less.

## 5.6 Luminosity Measurement

The primary physics goal of the FPD is to measure hard diffractive processes. Since the quadrupole spectrometers will have acceptance for elastic events, it is possible that the FPD could also be used to reduce the luminosity uncertainties for all DØ processes. The dominant uncertainty in the 5.4% luminosity error of Run I [45] was the discrepancy between the total cross section values measured by the CDF and E710 collaborations [46, 47]. It should be possible for us to accurately measure the total cross section, and also to have a run-by-run determination of the luminosity using the FPD.

### 5.6.1 Total Cross Section

The luminosity independent method [46] is the best way to measure the total cross section using the FPD, since it does not require very low $|t|$ acceptance. This method combines the definition of the total cross section (Eq. 11)

$$\sigma_T = \frac{N_{el} + N_{inel}}{\mathcal{L}} \tag{11}$$

with the optical theorem

$$\sigma_T^2 = \frac{16\pi \frac{dN(t=0)}{dt}}{\mathcal{L}(1+\rho^2)} \tag{12}$$

and the relation $(dN(t=0)/dt) = BN_{el}$ to obtain

$$\sigma_T = \frac{16\pi B N_{el}}{(N_{el} + N_{inel})(1+\rho^2)} \tag{13}$$

where $N_{el}$ is the extrapolated number of elastic events, $N_{inel}$ is the number of inelastic events, $B$ is the slope of the elastic $|t|$ distribution, and $\rho$ is the ratio of the real to imaginary part of the elastic scattering amplitude.

In a low luminosity special run with extra beam scraping, it will be possible to obtain a $|t|_{MIN} \approx 0.15$ GeV$^2$. CDF and E710 are in very good agreement for the elastic slope in the region $|t| < 0.15$ GeV$^2$ $(B_1)$, with a virtually identical central value yielding a world average measurement

of $B_1 = 16.99 \pm 0.22$ GeV$^{-2}$. For a 50,000 event special run, the largest error in the measurement should be about 1.5% from the extrapolation to $t = 0$. The contribution of the $\rho$ error to the cross section is small, and the Level Ø counters will be used to accurately measure $N_{inel}$. The slope in the region $0.15 < |t| < 0.6$ GeV$^2$ ($B_2$) is flatter than $B_1$, and is measured to be $B_2 = 16.3 \pm 0.5$ GeV$^{-2}$ [46]. This 3% error could be reduced to about 0.5% during this run.

The elastic cross section is roughly 20 mb, and about 8% of the events have $|t| > 0.15$ GeV$^2$, giving an effective cross section of 1.6 mb. Assuming a $\phi$ acceptance of 20% and a luminosity of $1 \cdot 10^{28}$ cm$^{-2}s^{-1}$ gives a rate of 3 Hz. A five hour run will thus give 50,000 elastic events. Note that this will be a one-time run which could be done after all of the properties of the FPD are well-understood, and would consequently not require any dedicated setup time. With a data sample of 50,000 good elastic events it should be possible to measure the total cross section to an accuracy of about 2%.

### 5.6.2 Run-by-run Luminosity Monitor

It will also be possible to use the FPD to determine the luminosity on a run-by-run basis by counting elastic events and using previously measured values for $\sigma_T$, $B_1$, and $B_2$, or values measured by DØ in the special run described above. The accuracy will be much better in the latter case. For $|t| > 0.5$ GeV$^2$ the effective elastic cross section is 0.8 $\mu$b (applying a $|t|$ acceptance factor of 0.0002 and a $\phi$ acceptance of 20%). For a typical luminosity of $4 \cdot 10^{31}$ cm$^{-2}s^{-1}$, the single interaction elastic rate will be about 10 Hz. A special elastic scattering data stream which writes out selected detector information at about 1 Hz will yield 10,000 elastic events per run. This will give a 1% statistical uncertainty, so a few percent measurement on a run-by-run basis will likely be obtainable. These events would also be used for FPD calibration.

The background to elastics will be the overlap of one $p$ and one $\overline{p}$ halo event, which will have a rate of $R = 1.7 \cdot 10^6 \cdot (0.0008)^2 = 1$ Hz where 1.7 Mhz is the crossing rate and 0.0008 is the halo suppression factor from Sec. 5.3.2. A cut on the timing of the trigger scintillators in the two arms will reduce this background to a few percent of the elastic rate.

## 5.7 Running with 132 ns Bunch Spacing

For the studies presented above, we have been considering 36 bunch (396 ns) running. At some point during Run II, we expect to switch to 132 ns running (see Sec 3.3.3). The FPD will be able to run effectively in this mode. We will be using standard DØ data structures which were designed to handle 132 ns. The time for a Level 1 decision will not be changed. The multiple interaction profile should be quite similar to the 396 ns mode, since at a given luminosity there are three times fewer interactions at 132 ns, but this improvement is offset by the increased luminosity. As shown in Sec 3.3.3, the overall acceptance is comparable (within a factor of two). The early time rejection of halo might not be as effective as in the 36 bunch scenario, but the amount of halo per bunch will be reduced, and halo can easily be expunged by a slight increase in the $\xi$ cut.

## 5.8 Data Taking Summary

The addition of the FPD triggers will have little impact on backgrounds at DØ or the overall trigger rates, at most at the few percent level. Many handles exist to reject backgrounds to hard diffraction, and with early data an optimized trigger list can be formed. Large data samples can be obtained with little background, and will allow us to study the full physics menu discussed in Sec. 2.

# 6 Accelerator Modifications

Accelerator modifications consist of moving the quadrupoles closer to the interaction point and inserting the Roman pots into the region of the electrostatic separators.

There are several issues that must be considered before moving the quadrupoles including the effect on Tevatron operation, shielding at DØ, and the method for mechanically supporting the $Q_4$ quadrupole.

The effects on the lattice are fairly minor and appear to be beneficial. As mentioned earlier, moving the quadrupoles necessitates a few percent change in the gradients in order to properly retune the Tevatron. This is an acceptable change as the gradients remain below the limit of 140 Tesla/meter for a modest two-thirds of a meter shift in the quadrupoles. This change also allows the gradient on the $Q_5$ quadrupole to be set at an acceptable level, even with 1 TeV operation, which is not the case for the dispersion-free lattice with the quadrupoles in the current position [37].

The technical aspects of moving the magnets and supporting the $Q_4$ quadrupole must be studied in detail. The location of the quadrupoles will have an impact on the design of the extra shielding that will be implemented in Run II to reduce backgrounds to the muon system. In this context, DØ engineers have studied shielding design with the quadrupoles in the nominal position and moved one meter closer to the interaction region. The studies show that the shielding can be just as effective in either scenario. They also show that supporting the quadrupoles can be done while maintaining or even improving the current deflection of the quadrupole without a major redesign. This can be accomplished by reinforcing and lengthening the shelf that extends off the main girder that currently supports the quadrupole. A final study and cost estimate should be prepared by the Beams Division engineers, but preliminary results are promising.

The modifications to the separator bypass also require a detailed Beams Division engineering study. It does not seem to be a problem to add the pots as long as a sufficient vacuum is maintained. To this end we plan to have vacuum valves on either end of the pots as shown earlier in Fig. 9, so that the separator vacuum and cleanliness are not compromised by the installation of the pots. It would also be easy to remove a station during a short access (and replace it with a spare or a standard section of beam pipe) in the unlikely event of some problem with the pots.

# 7 Conclusions

For the next ten years the Tevatron offers the best possibility to understand pomeron exchange and the transition between non-perturbative and perturbative QCD. The addition of the FPD would greatly increase the physics reach of the hard diffractive physics program with no negative impact on the current DØ physics program. We stress that the measurements of jets and particles will be done with the upgraded DØ detector, which will be very well suited to this purpose. The FPD will be used to ensure that we have large diffractive data samples and that we can divide them into $\xi$ and $|t|$ bins. It will allow accurate determination of pomeron structure and hard diffractive cross sections, permitting us to greatly expand the knowledge of the field of hard diffraction.

**ACKNOWLEDGEMENTS**

We thank our colleagues in the D/O/ Collaboration for their support in preparing this document. We thank the staffs at Fermilab and collaborating institutions for their contributions to this work, and acknowledge support from the Department of Energy and National Science Foundation (U.S.A.), CNPq and CAPES (Brazil).

We would like to thank numerous members of the Beams Division for their encouragement, help, and many useful discussions. Specifically, Sasha Drozhdin did many background simulations in conjunction with Nikolai Mokhov, and the proposal would not have been possible without them; Mike Martens provided us with tracking programs and showed us how to use them; Carol Johnstone and John Johnstone helped us with lattice issues; Stan Pruss also was a valuable resource.

Ernie Villegas and Andy Stefanik performed studies showing that the supporting the moved-in quadrupole was feasible. Thanks to Newton Oliveira and Iuri Pepe of Instituto de Fisica da Universidade da Bahia/Universidade da Bahia who worked on the Roman pot design. Kurt Krempetz performed initial Roman pot cost estimates. Thanks also to Mike Albrow, Hirofumi Ikeda, and Phil Melese of the CDF Collaboration for discussions about the CDF Tokyo pots. Thanks to Carlos Avila of E811 for many useful discussions about their Roman pots and techniques.

## References


[1] G. Alberi and G. Goggi, Physics Reports **74**, 1 (1981); K. Goulianos, Physics Reports **101**, 169 (1983). A. Donnachie and P.V. Landshoff, Nucl. Phys. B **244**, 322 (1984); B **267**, 690 (1986).

[2] M. Albrow *et al.*, "QCD Subgroup on Diffractive and Forward Physics", *Proceedings of 1996 DPF Study on New Directions for High-energy Physics (Snowmass '96)*, Snowmass CO (1996).

[3] G. Ingelman and P. Schlein, Phys. Lett. B **152**, 256 (1985).

[4] R. Bonino *et al.* (UA8 Collaboration), Phys. Lett. B **211**, 239 (1988).

[5] A. Brandt *et al.* (UA8 Collaboration), Phys. Lett. B **297**, 417 (1992).

[6] A. Brandt *et al.* (UA8 Collaboration), Nucl. Instrum. and Meth. in Phys. Res. A **327**, 412 (1993).

[7] M. Derrick *et al.* (ZEUS Collaboration), Phys. Lett. B **315**, 481 (1993).

[8] T. Ahmed *et al.* (H1 Collaboration), Nucl. Phys. B **429**, 477 (1994).

[9] H. Chehime and D. Zeppenfeld, preprint MAD/PH/814 (1994).

[10] A. Doyle, *Workshop on HERA Physics, "Proton, Photon, and Pomeron Structure"*, GLAS-PPE/96-01.

[11] A. Brandt (DØ Collaboration) *Proceedings of the 11th Topical Workshop on Proton-Antiproton Collider Physics*, Abano Terme, Italy, 1996.

[12] P. Melese (CDF Collaboration) *Proceedings of the 11th Topical Workshop on Proton-Antiproton Collider Physics*, Abano Terme, Italy, 1996; *Proceedings 1996 Divisional Meeting of the Division of Particles and Fields*, Minneapolis, MN, 1996.

[13] F. Abe *et al.* (CDF Collaboration), Phys. Rev. Lett. **78**, 2698 (1997).

[14] S. Abachi *et al.* (DØ Collaboration), Phys. Rev. Lett. **72**, 2332 (1994).

[15] F. Abe *et al.* (CDF Collaboration), Phys. Rev. Lett. **74**, 855 (1995).

[16] S. Abachi *et al.* (DØ Collaboration), Phys. Rev. Lett. **76**, 734 (1996).

[17] M. Derrick *et al.* (ZEUS Collaboration), Phys. Lett. B **369**, 55 (1996).

[18] J. Pumplin Phys. Rev. D **50**, 6811 (1994); I.M. Dremin, preprint FIAN TD-6, (1994).

[19] M. Derrick *et al.* (ZEUS Collaboration), Phys. Lett. B **356**, 129 (1995).

[20] K. Goulianos, Phys. Lett. B **358**, 379 (1995).

[21] F. Abe *et al.* (CDF Collaboration), Phys. Rev. D **50**, 5535 (1994).

[22] F. Abe *et al.* (CDF Collaboration), Phys. Rev. D **50**, 5518 (1994).

[23] L. Frankfurt and M. Strikman, Phys. Rev. Lett. **63**, 1914 (1989); **64** 815 (1990).

[24] G. Alves, E. Levin, and A. Santoro, Phys. Rev. D **55**, 2683 (1997).

[25] J. Pumplin, Phys. Rev. D **52**, 1477 (1995).

[26] A. Berera and J. Collins, Nucl. Phys. B **474**, 183 (1996).

[27] A. Bialas and P.V.Landshoff, Phys. Lett. B **256**, 540 (1991).

[28] P. Melese (CDF Collaboration) *Proceedings of the 5th International Workshop on Deep Inelastic Scattering and QCD (DIS 97)*, Chicago, IL, April 14-18 1997.

[29] E. Gotsman, E.M. Levin, U. Maor, Phys. Lett. B **353**, 526 (1995).

[30] M. Tamada, Nuovo Cimento **41B**; C.M.G. Lattes, Y. Fujimoto, and S. Hasegawa, Phys. Rep. **65**, 151 (1980).

[31] K. Goulianos, *Proceedings of the Workshop on Physics Simulations at High Energies*, Madison, WI, May 1986.

[32] J.C. Collins, L. Frankfurt, and M. Strikman, Phys. Lett. B **307**, 161 (1993).

[33] P. Bruni and G. Ingelman, DESY 93-187; Proceedings of the Europhysics Conference on HEP, Marseille 1993, 595.

[34] H.-U. Bengtsson and T. Sjöstrand, Comp. Phys. Comm. **46**, 43 (1987); T. Sjöstrand, CERN-TH.6488/92.

[35] "Proposal for Hard Diffraction Studies in CDF", (CDF Collaboration), CDF/CDFR/2940, (1995).

[36] Tracking program provided by M. Martens, L. Michelotti.

[37] J.A. Johnstone, "Report to the Low Beta Study Group", Fermilab Internal Report, (1994).; J.A. Johnstone, private communication (1996).

[38] A. Brandt, A. Drozhdin, and N. Mokhov, "The DØ Roman Pots Detector Beam Loss Simulations", unpublished (1997).

[39] M. Albrow (CDF Collaboration), private communication.

[40] P.P. Bagley (Beams Division), private communication.

[41] P.P. Bagley *et al.*, "Summary of the TeV33 Working Group", *Proceedings of 1996 DPF Study on New Directions for High-energy Physics (Snowmass '96)*, Snowmass CO (1996).

[42] C. Kim and A. Bross, "Attenuation and Radiation Damage Studies of Multi-clad Optical Fiber", unpublished (1996).

[43] K.H. Streng, Phys. Lett. B **166**, 443 (1986).

[44] A. Brandt *et al.* (UA8 Collaboration), "Cross Section Measurements of Hard Diffraction at the SPS Collider", Submitted to Phys. Lett.

[45] "Improvement to the DØ Luminosity Monitor Constant", J. Bantly *et al.*, FERMILAB-TM-1930 (1995).

[46] N. Amos *et al.* (E710 Collaboration), Phys. Lett. B **243**, 158 (1990).

[47] F. Abe *et al.* (CDF Collaboration), Phys. Rev. D **50**, 5550 (1994).